Pereira, ALJ.; Gomis, O.; Sans, JA.; ALFONSO MUÑOZ; Pellicer-Porres, J.; Manjón Herrera, FJ.; Beltran, A.... (2014). Pressure effects on the vibrational properties of alpha-Bi2O3: an experimental and theoretical study. Journal of Physics: Condensed Matter. 26(22):225401-1-225401-15. doi:10.1088/0953-8984/26/22/225401.

Pressure effects on the vibrational properties of α-Bi_2O_3: an experimental and theoretical study

A.L.J. Pereira[1,*], O. Gomis[2], J.A. Sans[1], J. Pellicer-Porres[3], F.J. Manjón[1], A. Beltran[4], P. Rodríguez-Hernandez[5], A. Muñoz[5]

[1]*Instituto de Diseño para la Fabricación y Producción Automatizada, MALTA Consolider Team, Universitat Politècnica de València, 46022 Valencia, Spain*

[2] *Centro de Tecnologías Físicas: Acústica, Materiales y Astrofísica, MALTA Consolider Team, Universitat Politècnica de València, 46022 Valencia, Spain*

[3] *Departamento de Física Aplicada-ICMUV, MALTA Consolider Team, Universitat de València, 46100 Burjassot (Valencia), Spain*

[4] *Departament de Química Física i Analítica, MALTA Consolider Team, Universitat Jaume I, 12071Castelló, Spain*

[5]*Departamento de Física Fundamental II, Instituto de Materiales y Nanotecnología, MALTA Consolider Team, Universidad de La Laguna, 38205 La Laguna (Tenerife), Spain*

* Corresponding author: andeje@upvnet.upv.es

Abstract. We report an experimental and theoretical high-pressure study of the vibrational properties of synthetic monoclinic bismuth oxide (α-Bi_2O_3), also known as mineral bismite. The comparison of Raman scattering measurements and theoretical lattice-dynamics *ab initio* calculations is key to understand the complex vibrational properties of bismite. On one hand, calculations help in the symmetry assignment of phonons and to discover the phonon interactions taking place in this low-symmetry compound which shows considerable phonon anticrossings; and, on the other hand, measurements help to validate the goodness of first-principles calculations of this compound. We have also studied the pressure-induced amorphization (PIA) of synthetic bismite occurring around 20 GPa and showed that it is reversible below 25 GPa. Furthermore, a partial temperature-induced recrystallization (TIR) of the amorphous sample can be observed above 20 GPa upon heating to 200ºC, thus evidencing that PIA at room temperature occurs because of the inability of the α phase to undergo a phase transition to a high-pressure phase. Raman scattering measurements of the TIR sample at room temperature during pressure release have been performed. The interpretation of these results under the light of *ab initio* calculations of the candidate phases at high pressures has allowed us to tentatively attribute the TIR phase to the recently found high-pressure hexagonal HPC phase and to discuss its lattice dynamics.

Keywords: sesquioxides, hydrostatic pressure, amorphization, lattice dynamics, *ab initio* calculations

PACS numbers: 62.50.-p, 63.20.dk, 71.15.Mb, 78.30.Hv

1. Introduction

Bismuth trioxide (Bi_2O_3) is the most industrially important compound of bismuth since it is one of the common starting points for bismuth chemistry, including the synthesis of many good ionic conductors **[1-3]**, thermoelectric and ferroelectric materials **[4, 5]**, and recently discovered topological insulators and superconductors based on Dirac-cone science **[6-12]**. Bi_2O_3 can also be used to produce the "Dragon's eggs" effect in fireworks **[13]**, for gas sensors **[14,16]**, and in solid oxide fuel cells **[17-20]**. Besides, Bi_2O_3 is also an interesting candidate for several applications in optical telecommunication, processing devices **[21,22],** ecological *lead-free* glasses **[23-25]** and visible light responsive photocatalysis [**26,27**].

One of the most intriguing properties of Bi_2O_3 is its wide variety of polymorphs: i) bismite mineral (α-Bi_2O_3) with monoclinic $P2_1/c$, No. 14 space group (SG) **[28]**; ii) the rare tetragonal sphaerobismoite mineral (β-Bi_2O_3) with SG $P\text{-}42_1c$, No. 114 **[29]**; iii) the body-centered cubic γ-Bi_2O_3 (SG $I23$, No. 197) **[30-32]**; iv) the high-temperature cubic fluorite-type δ-Bi_2O_3 (SG $Fm\text{-}3m$, No. 225) **[33]**; v) the orthorhombic ε-phase (SG *Pbnb*, No. 56); and vi) the triclinic ω-phase (SG P-1, No 2) **[34,35]**. Recently, new phases of Bi_2O_3 were found on increasing pressure. Starting with the α phase, Ghedia *et al*. **[36]** identified two different metastable polymorphs of Bi_2O_3 at ambient conditions after compressing the sample up to 6 GPa and heating at 880 ºC for 30 min: trigonal HP-Bi_2O_3 (SG $P31c$, No. 159) and monoclinic R-Bi_2O_3 (SG $P2_1/c$, No. 14). It must be added that a hexagonal polymorph at high pressure (HPC-Bi_2O_3 with SG $P6_3mc$, No. 186) was recently obtained after pressurizing HP-Bi_2O_3 **[37]**.

It is well known that lattice dynamics determines many physical properties of crystals which can be nicely simulated by *ab initio* calculations **[38]**. For that purpose, calculations need to be validated with the most exhaustive experimental data, being the complete experimental information on the lattice

dynamics along the whole Brillouin zone (BZ) only obtained by means of inelastic x-ray or neutron scattering. However, this method is only effective for simple crystals with a small number of phonon branches **[39,40]**, which is not the case of monoclinic α-Bi_2O_3 with 60 phonon branches in the small spectral range of 50–550 cm^{-1} **[41]**. Therefore, Raman scattering and infrared (IR) spectroscopy measurements of α-Bi_2O_3 allow obtaining crucial information on vibrational modes at the BZ center, Γ, in order to validate lattice dynamics calculations. In this context, several Raman scattering and IR spectroscopy measurements of monoclinic α-Bi_2O_3 at 1 atm have been reported **[42-48]**, but only a few have made some detailed comments on its complex lattice dynamics **[41,45-47]**, being the vibrational properties of α-Bi_2O_3 not well understood yet. In this context, the application of pressure allows obtaining a different perspective since pressure allows modifying interatomic distances which in turn lead to changes of the structural and lattice dynamical properties of solids. Therefore, the theoretical simulation of the lattice dynamics of solids under pressure and its comparison with experiments allows checking the goodness and extent of the approximations considered in the calculations. Very few works have been devoted to the study of the properties of α-Bi_2O_3 under pressure **[49-51]** and only one work reported the pressure dependence of the Raman-active modes of α-Bi_2O_3 **[49]**. In particular, lattice-dynamics *ab initio* calculations of α-Bi_2O_3 have not been reported yet to our knowledge. This information is critical to understand the properties of this material in order to turn this knowledge into technological devices.

On the other hand, the application of pressure leads to changes in the structural and dynamical properties in materials which may cause mechanical or dynamical instability of the original structure. In this sense, it has been published that α-Bi_2O_3 undergoes a pressure-induced amorphization (PIA) around 20 GPa depending on the quality of the material and the stresses at high pressures **[49,51]**. A large number of experimental and theoretical studies have been published about the fascinating world of PIA

in many materials and its connection to negative thermal expansion, melting and glass formation. PIA has been recently explained as a mechanical melting driven by elastic or lattice instabilities **[52-54]** and different mechanisms, still not well understood, have been proposed where defects and non-hydrostatic effects may play a significant role. In particular, it has been proposed that PIA is a consequence of the frustrated transition from a parent crystalline phase to another crystalline phase **[55]**; however, this hypothesis is still under debate and no study on the PIA of α-Bi_2O_3 has been performed yet.

In our aim to perform a systematic study of the structural and vibrational properties of Bi_2O_3 polymorphs under pressure at room temperature, we report in this work a detailed experimental and theoretical study of the vibrational properties of α-Bi_2O_3 up to 25 GPa. Experimental and theoretical pressure coefficients of the vibrational modes of the monoclinic phase are provided and compared with previous results. Theoretical calculations of the phonon dispersion curves and density of states of α-Bi_2O_3 at 1 atm are reported which have allowed us to discuss the nature of their complex vibrational properties including the anticrossing of several phonon branches. Furthermore, we report a study of the PIA of α-Bi_2O_3 at room temperature above 20 GPa. We have found that PIA is reversible below 25 GPa and that annealing the amorphous sample (after applying pressure above 20 GPa) at ~200^{o}C showed a temperature-induced recrystalization (TIR) of the sample. Therefore, our results support that PIA of α-Bi_2O_3 at room temperature is due to a frustrated crystalline phase transition. The monitoring of the TIR phase behavior on pressure by means of Raman scattering measurements have allowed us to report the pressure dependence of its Raman-active modes and discuss its lattice dynamics as well as to discuss the possible structure of the TIR phase.

2. Experimental Method

Synthetic α-Bi_2O_3 samples used in the present experiments were the same used in a previous structural study under pressure **[51]** and were purchased from Sigma-Aldrich Inc. with grade purity

higher than 99.9%. Raman scattering measurements at room temperature were performed in backscattering geometry exciting with a HeNe laser (6328 Å line) with a power of less than 10 mW in the source to avoid sample heating. The signal was collected by a Horiba Jobin Yvon LabRAM HR microspectrometer equipped with a thermoelectrically-cooled multichannel charge-coupled device detector which allows a spectral resolution better than 2 cm^{-1}. The experimental phonons have been analyzed by fitting, when possible, Raman peaks with a Voigt profile (Lorentzian convoluted with a Gaussian), where the Gaussian linewidth (1.6 cm^{-1}) has been fixed to the experimental setup resolution **[56]**.

In order to perform high-pressure Raman scattering measurements, samples were loaded together with a 16:3:1 methanol-ethanol-water (MEW) mixture in a membrane-type Chervin-Le Toullec-type diamond anvil cell (MDAC) with diamond culets of 500 μm in diameter. Ruby chips evenly distributed in the pressure chamber were used to measure pressure by the fluorescence method **[57]**. Two high-pressure experiments were performed. In the first one, pressure was increased from 1 atm up to 25 GPa and then decreased to 1 atm again in order to check the reversibility of the PIA process taking place above 20 GPa. In the second one, pressure was increased from 1 atm to 20.5 GPa and the MDAC was heated in order to induce a TIR in the sample. The internal temperature was estimated by the $^7D_0$–$^5F_0$ fluorescence line of SrB_4O_7:Sm^{2+} that was evenly distributed in the pressure chamber **[58]**. Upon increasing the external temperature of the MDAC to 300ºC the temperature and pressure in the sample chamber increased to 200 ºC and 22.2 GPa, respectively. After 3 hours the heating system was disconnected, allowing the system slowly return to room temperature while maintaining a constant pressure (22.2 GPa). Subsequent Raman scattering measurements on downstroke from 22.2 GPa down to 1 atm were performed at room temperature. In both experiments the pressure was increased with

increments of 1-1.5 GPa and after the pressure increase we waited for ~5 min before perform the measurement.

3. Theoretical details

Ab initio total-energy calculations have been performed within the framework of density functional theory (DFT) **[59]**. The VASP package has been used to carry out calculations with the pseudopotential method and the projector augmented wave (PAW) scheme, which replace the core electrons and make smoothed pseudovalence wave functions **[60]**. For Bismuth, 15 valence electrons ($5d^{10}6s^{2}4p^{3}$) are used, whereas for Oxygen, 6 valence electrons ($2s^{2}2p^{4}$) are used. Highly-converged results were achieved by extending the set of plane waves up to a kinetic energy cutoff of 520 eV. The exchange-correlation energy was taken in the generalized gradient approximation (GGA) with the PBEsol prescription **[61]**. A dense Monkhorst-Pack grid (6x4x4) of 42 k-special points was used to perform integrations along the BZ in order to obtain very well converged energies and forces. At each selected volume, the structures were fully relaxed to their equilibrium configuration through the calculation of the forces on atoms and the stress tensor. In the relaxed configurations, the forces on the atoms are less than 0.006 eV/Å and deviations of the stress tensor from a diagonal hydrostatic form are less than 0.1 GPa.

In order to verify the influence of the spin-orbit coupling (SOC) on the Raman frequencies of the α-Bi_2O_3 we performed calculations with and without the SOC considering a pressure of 18.1 GPa. Comparing the two calculations, we observed only a slightly softening of the phonon frequencies (maximum difference of 5 cm^{-1} for the highest-frequency modes with respect to the calculation without SOC) like that reported by Sklyadneva *et al* in BiTeI and BiTeCl **[62]**. Furthermore, in previous works with Bi_2Se_3 and Bi_2Te_3 **[63,64]** we also performed calculations with and without considering the SOC

and the Raman frequencies and their pressure coefficients did not show important differences. On the other hand, calculations taking into account the SOC are computationally very demanding since they require the deactivation of symmetry in the program thus leading to very long computational time. Finally, we want to note also that SOC calculations in Bi_2O_3 are even more computationally demanding than those in Bi_2Se_3 or Bi_2Te_3, because of the lower symmetry of α-Bi_2O_3 and the larger number of atoms in the unit cell. For these reasons, calculations reported in this work do not include the SOC.

Lattice-dynamics calculations were performed at the zone centre (Γ point) of the BZ. Highly converged results on forces are required for the calculation of the dynamical matrix using the direct force constant approach **[65]**. The construction of the dynamical matrix at the Γ point of the BZ involves separate calculations of the forces in which a fixed displacement from the equilibrium configuration of the atoms within the primitive cell is considered. The number of such independent displacements in the analysed structures is reduced due to the crystal symmetry. Diagonalization of the dynamical matrix provides the frequencies of the normal modes. Moreover, these calculations allow one to identify the symmetry and eigenvectors of the vibrational modes in each structure at the Γ point. In order to obtain the phonon dispersion and the phonon density of states (DOS), we performed similar calculations using a 2x2x2 supercell containing 160 atoms, which allows obtain exactly the phonon dispersion at *k* points commensurate with the supercell size **[65]**. The calculation of some pressures was also performed with a 3x3x3 supercell with 540 atoms but no significant difference with respect to the 2x2x2 supercell was observed (~0.09%) in the phonon frequencies. However, the computational time increased using the 3x3x3 supercell. For this reason we decided to use the 2x2x2 supercell to perform the phonon dispersion calculation.

4. Results and discussion

4.1 High-pressure behavior of Raman-active modes in α-Bi_2O_3

The monoclinic structure of α-Bi_2O_3 at room pressure has two Bi atoms located at two independent 4*e* Wyckoff sites and three O atoms located at three independent 4*e* Wyckoff sites (see **Fig. 1(a)**). This structure has two different coordination numbers for Bi to O atoms: Bi1 has five-fold coordination and Bi2 has six-fold coordination. The Bi1 polyhedron is like a distorted pyramid with Bi-O bond lengths varying from 2.07 to 2.63 Å, while the Bi2 polyhedron is a very distorted octahedron with Bi-O bonds varying from 2.13 to 2.79 Å. Furthermore, the structure of α-Bi_2O_3 can be described as succession of slightly distorted layers of Bi atoms and oxide ions parallel to the plane (100) (see **Fig. 1(a)**) **[35]**.

Since there are four formula units in the primitive cell of α-Bi_2O_3, group theory predicts 60 normal vibrational modes at the BZ center **[66]**:

$$\Gamma = 15(A_g + B_u) + 15\,(B_g + A_u) \quad (1)$$

where A modes mainly correspond to vibrations of atoms along the *b* axis of the monoclinic structure, B modes mainly correspond to vibrations in the *ac* plane perpendicular to the *b* axis, and the g and u represent the symmetric and antisymmetric modes with respect to the centre of inversion. In summary, there are thirty Raman-active modes ($\Gamma_{Raman} = 15A_g + 15B_g$), twenty-seven infrared-active (IR) modes ($\Gamma_{IR} = 14A_u + 13B_u$) and three acoustic modes ($\Gamma_{acoustic} = A_u + 2B_u$).

Figure 2(a) shows the Raman spectra of α-Bi_2O_3 at selected pressures up to 25 GPa. It can be observed that Raman modes below 200 cm^{-1} are rather narrow while above 200 cm^{-1} are very broad. The broadening of Raman modes was explained by Betsch and White as due to positional disorder resulting

from the random orientation of the lone-pair orbitals of Bi atoms **[41]**; on the other hand, Denisov *et al.* commented that this could be due to strong anharmonic coupling related to O atoms **[46]**. The large number of Raman-active modes and the broadening of many of them make some modes hard to identify at room conditions because there are several close Raman peaks which overlap as already commented in previous references **[41,46]**. Fortunately, pressure causes a splitting of several Raman bands with different pressure coefficients and allows us to assign the pairs of modes near 93, 210 and 445 cm^{-1} by fits to Voigt's functions. On the opposite, a weak mode located at 160 cm^{-1} at 1 atm disappears with increasing pressure because it calculated pressure coefficient (the experimental could not be estimated) is smaller than the one of the mode with lowest frequency (see **Table I**). Taking into account these considerations, it was possible to identify twenty vibrational modes at room pressure and twenty-one modes at high pressures out of the thirty expected modes. As can be observed in **Table I**, our experimental and theoretical frequencies for the Raman-active modes at 1 atm are in good agreement and also agree with those already reported in the literature **[41-46]**. We have noted that most of the Raman-active modes detected in our powder sample correspond to modes with A_g symmetry in good agreement with previous authors **[41,46]**. This result is likely due to the stronger change of polarizability related to modes with vibrations along the *b* axis than in the *ac* plane and contrasts with the behavior of IR-active modes since it has been reported that B_u modes show larger intensity than A_u modes because of the larger dipolar moment of vibrations in the *ac* plane than along the *b* axis **[47]**.

Figure 2(b) shows the experimental and theoretical pressure dependence of the Raman-active mode frequencies of α-Bi_2O_3 up to 20 GPa. It can be observed that many A_g modes are similar in frequency to B_g modes; i.e., they seem to come in pairs. This was previously noted **[41,45]** and we confirm that it also occurs for IR-active modes according to our theoretical calculations (see **Figure 10** in the Appendix). However, the most notable result of the effect of pressure on the vibrational modes is

that the frequency of Raman-active modes between 380 and 450 cm^{-1} show a non-monotonous pressure dependence which is confirmed by both our experimental and theoretical results (see **Figs. 3(a)** and **3(b)** for more detail). This result was not addressed in previous literature **[49]** and we will discuss it later.

In order to explain the vibrational properties of α-Bi_2O_3, let us begin by establishing the symmetry of the different Raman-active modes we have measured. In this context, the good agreement between our experimental and theoretical frequencies and pressure coefficients (see **Fig. 2(b)** and **Table I**) has allowed us to make a tentative assignment of the symmetry of the observed Raman peaks. It must be stressed that the symmetry assignment to experimental Raman peaks in the region from 400 to 600 cm^{-1} is not easy because many peaks overlap due to: i) the large number of Raman modes in this region, as indeed evidenced by our theoretical calculations, and ii) the large linewidths of the Raman peaks, as already commented. **Table I** summarizes the zero-pressure experimental and theoretical frequencies and their pressure coefficients for the Raman-active modes as well as their symmetries. Results previously reported for powder and single crystal samples are also shown in **Table I** for comparison **[49]**. In general, there is a good agreement between our measurements and those previously reported. However, some of our symmetry assignments, which have been made on the basis of the comparison with theoretical results, do not agree with those proposed by Chouinard *et al.* **[49]**, which, in turn, are based in the assignment previously reported by Denisov *et al.* **[46]**. On one hand, Raman peaks observed by us at 93, 151 and 528 cm^{-1} and by Chouinard *et al.* at 95, 153 and 533 cm^{-1}, and which were previously assigned as A_g modes, have a frequency and pressure dependence which is more consistent with B_g modes according to our theoretical calculations. On the other hand, Raman peaks observed by us at 93, 329 and 448 cm^{-1} and by Chouinard *et al*. at 97, 144, 334 and 450 cm^{-1}, which were previously assigned as B_g modes, are more consistent with A_g modes according to our calculations. Note that in **Table I** we have shown Chouinard *et al.* results with our proposed symmetry.

In order to better understand the complex vibrational properties of α-Bi_2O_3 we have performed calculations of the phonon dispersion curves and total and partial one-phonon DOS at 1 atm (see **Fig. 4(a)**). The *ab initio* calculated phonon dispersion curves are rather complex and in general show a larger *k*-dispersion than those previously reported by Denisov *et al.* which were calculated with a rigid-ion model **[46]**. Our total DOS shows a main minimum at 1 atm around 250 cm^{-1} that compares better with the experimental one at 260 cm^{-1} **[48]** than the one calculated by Denisov *et al.* (290 cm^{-1}) **[46]**. Similarly, our DOS shows the main peaks around 65, 90, 130, 205, 300, 340, 400-440 and 520 cm^{-1} which compare well with the experimental ones at 59, 102, 123, 200, 340, 400-460 and 530 cm^{-1} **[48]**. In agreement with Denisov *et al.*, our partial DOS shows that the vibrational modes up to 155 cm^{-1} are dominated by Bi movements with a small contribution of O. On the other hand, modes ranging from 155 cm^{-1} to 255 cm^{-1} have a significant contribution of both Bi and O atoms, but with a larger contribution of the O atoms. Finally, the vibrational modes with frequencies higher than 255 cm^{-1} are mainly due to displacement of the O atoms. Therefore, our results clearly show that the different contributions of Bi and O at different frequencies are directly related with the mass difference between the atomic species **[46]**.

Visualization of the *ab initio*-calculated vibrational modes of α-Bi_2O_3 at Γ with the J-Ice software **[67]** has allowed us further understanding the complex lattice dynamics of this compound. We have observed that in general the motion of atoms is very complex and no modes related to isolated molecular units can be identified in good agreement with Denisov *et al*. who commented it on the basis of the eigenvectors of the different vibrational modes **[46]**. Modes from 0 to 190 cm^{-1} can be tentatively classified as lattice modes due to large Bi movements, being many of them stretching modes of the Bi-Bi subunits. From 190 to 340 cm^{-1}, modes can be mainly described as bending modes of both BiO_5 and BiO_6 units. Between 340 and 450 cm^{-1} the classification of modes is extremely difficult and they seem

to be a combination of asymmetric stretching and bending modes of Bi-O bonds, while the few modes above 450 cm^{-1} can be classified mainly as stretching Bi-O modes.

Now that we have reviewed the lattice dynamical properties of α-Bi_2O_3 at room pressure, let us explain the non-linear and non-monotonous pressure dependence of the Raman frequencies between 380 cm^{-1} and 450 cm^{-1}, which are zoomed for A_g and B_g modes in **Figs. 3(a) and 3(b)**, respectively. In this respect, one could invoke the presence of non-hydrostatic stresses inside the MDAC. If this were the case a uniform increase of the full width at half maximum (FWHM) for all peaks above certain pressure should have been evidenced in **Fig. 5**. However, the FWHMs of different modes have a completely different pressure dependence. This is the expected result if the FWHM is related to its decay into other phonons according to its frequency with respect to maxima and minima of the two-phonon density of states **[68]** and there is no presence of important non-hydrostatic stresses. Moreover, our experimental frequencies show a pressure dependence which agrees with the ones exhibited by the theoretical calculations under ideal hydrostatic conditions. Instead, we think that the anomalous pressure dependence of the Raman-active modes shown in **Figs. 3(a)** and **3(b)** is caused by the occurrence of several anticrossings of Raman-active modes of the same symmetry lying in the same frequency region at the Γ point of the BZ **[69]**. Note that α-Bi_2O_3 has a complex vibrational scenario along the whole BZ where several anticrossings can be observed out of the BZ center in **Fig. 4(a)**. The anticrossings of both the Raman-active modes of A_g and B_g symmetry plotted in **Fig. 2(b)** can be better observed in **Figs. 3(a)** and **3(b)**, where dashed lines show the expected pressure dependence of the theoretical frequencies if no anticrossing would occur. Among the dashed lines, it can be observed in **Figs. 3(a)** and **3(b)** the presence of two soft modes, one A_g and one B_g, between 430 and 440 cm^{-1}; i.e., two modes with a negative pressure coefficient, whose frequency is slightly larger but close to other modes of the same symmetry with normal (positive) pressure coefficients. Consequently, a crossing of the soft modes with

the normal modes occurs at high pressures. However, such crossing cannot occur for two modes with the same symmetry, hence resulting in a pressure-induced phonon anticrossing **[70]**. It can be observed that on increasing pressure, in the pressure range between 1 atm and 20 GPa, the soft A_g mode undergoes up to three consecutive anticrossings with normal A_g modes, whereas the soft B_g mode undergoes two consecutive anticrossings with normal B_g modes. Noteworthy, a pressure-induced phonon anticrossing has been already observed in another sesquilateral compound with monoclinic structure like As_2S_3 **[71,72]**.

Finally, we want to note that the pressure-induced phonon anticrossings can also be observed in the IR-active modes of α-Bi_2O_3. Unlike the Raman modes of α-Bi_2O_3, the IR anticrossings of several A_u modes are observed in rather different frequency regions (near 300 cm^{-1} and between 400 and 500 cm^{-1}) as reported in **Fig. 10** in the Appendix. Note that only the IR-active TO modes are depicted in **Fig. 10** because the TO-LO splitting is expected to be very small because of the covalent character of the Bi-O bond **[41,46]**. **Table III** in the Appendix summarizes the calculated zero-pressure IR-active mode frequencies (only TO modes) and pressure coefficients in α-Bi_2O_3. We want to stress that our calculations for α-Bi_2O_3 yield the two IR-active modes with highest frequencies below 520 cm^{-1}; i.e., at similar but slightly higher frequencies than those of the highest Raman-active modes. Therefore, taking into account that calculated values slightly underestimate the experimental ones at high frequencies, our calculations suggest that the highest IR-active modes of α-Bi_2O_3 should be at most around 540 cm^{-1} as reported by Kuz'menko *et al.* **[47,48]** but in disagreement with other works which locate them around 580-590 cm^{-1} **[41,45]**. In this respect, it must be noted that our calculations agree with those based on the rigid-ion model who also found the highest frequency modes in the range below 540 cm^{-1} **[46]**. Note that some of the symmetries of our theoretical calculations, especially at high frequencies, differ from

those of Kuz'menko *et al*. This could be better discussed if future IR spectroscopy measurements at high pressures are performed.

4.2 Pressure-induced amorphization (PIA) of α-Bi_2O_3 and thermal annealing

Raman spectra shown in **Fig. 2(a)** can be assigned to synthetic α-Bi_2O_3 up to 19.5 GPa. Above 20 GPa, the Raman peaks lose their shapes and only broad bands are observed. The shape of the Raman spectrum does not present significant changes up to 25 GPa. This behavior is consistent with the PIA of the material that was also observed by Chouinard *et al.* at 21 GPa for powder samples and 24 GPa for a single crystal sample **[49]** and with the results of Pereira *et al.* on both synthetic and natural samples under different hydrostatic conditions **[51]**. On decreasing pressure down to 7 GPa, we observed a Raman spectrum which was similar to that at 25 GPa and which can be attributed to the amorphous phase. Below 7 GPa, peaks corresponding to the α phase start to reappear and the sample returns completely to the original structure at 1 atm, but showing broader Raman bands (see top of **Fig. 2(a)**). This result indicates that the PIA of α-Bi_2O_3 at room temperature is reversible up to 25 GPa. In this respect, it is important to stress that we did not perform any kind of annealing in the amorphous sample during the pressure release process. In fact, we perform Raman scattering measurements in different zones of the sample with different neutral density filters (we reduced the laser power even by a factor 100 in some zones) and checked that the main peaks of the α phase were observed in all zones irrespective of the incident laser power in order to ensure that the reversibility process was not related to accidental heating of the sample by the laser. Therefore, this result indicates that the recovery of the initial phase is not triggered by heating of the sample. This result contrasts with the results of Chouinard *et al.*, who observed metastability of the amorphous phase at 1 atm after pressurizing the α phase up to 30 GPa **[49]**. Moreover, they reported the recrystallization of the sample at 1 atm after exciting the

sample with a laser of ~10 mW (~2 mW at the pressure chamber) for a certain period of time. In this context, we have to note that in a previous structural study, a synthetic sample of α-Bi_2O_3 pressurized up to 40 GPa in the same conditions as that of the present work (using MEW as pressure-transmitting medium) did not return to the initial phase [**51**]. Therefore, altogether these results point to the existence of a maximum pressure around 25-30 GPa beyond which the amorphous phase of Bi_2O_3 does not return to the α phase on releasing pressure at room temperature and heating is necessary to trigger the recrystallization process of the α phase.

In a recent structural study **[51]**, it was shown that the PIA of α-Bi_2O_3 near 20 GPa seems to be related with a frustrated phase transition to a more stable crystalline polymorph at high pressures and which was proposed to be the HPC phase reported by Locherer *et al*. **[37]**. This hypothesis was based on two facts: i) the HPC phase is the only one of the known polytypes of Bi_2O_3 which is competitive with the α phase at pressures around 20 GPa, and ii) the experimental structural parameters of the α phase near 20 GPa were found to be close to those of HPC-Bi_2O_3. In Ref. 51 it was suggested that the PIA process could be driven by a frustrated phase transition from the α to the HPC phase because of the existence of a kinetic energy barrier between both structures that impeded the phase transition and that cannot be overcome only by applying pressure at room temperature. According to this view, the amorphous phase would be a metastable phase which is energetically more stable and kinetically advantageous when compared to the high-pressure polymorph. However, the PIA mechanism in α-Bi_2O_3 is not fully clear yet, being necessary more elaborate models to understand this process.

In order to verify the above hypothesis regarding the frustration of the α to HPC phase transition and to shed light onto the PIA process of α-Bi_2O_3, we performed a second experiment where the powder sample was pressurized slightly above 20 GPa and then moderately heated (~200 ºC in the pressure chamber) to provide additional thermal energy and induce a temperature-induced recrystallization (TIR)

of the amorphous sample. **Fig. 6** shows the Raman spectra at room temperature around 22 GPa before and after thermal annealing at 200 ºC for 3 h. As it can be observed, new Raman peaks were detected after thermal annealing. The most notable peaks of the high-pressure crystalline phase corresponding to the TIR sample in **Fig. 6** are observed around 188, 196 and 293 cm^{-1}. However, a more detailed analysis of the Raman spectra of the TIR sample allows detecting up to fourteen Raman bands after deconvolution of the Raman signal using Voigt functions (they can be better evidenced by following their pressure dependence as will be commented later).

In order to get information on the high-pressure crystalline phase of the TIR sample and its metastability at room conditions and in order to check whether or not it could correspond to the HPC phase, we performed Raman scattering measurements of the TIR sample at room temperature on releasing pressure down to 1 atm (see Raman spectra in **Fig. 7**). From 22.2 to 14.3 GPa, the intensity of the Raman peaks increase what made easier the identification of the vibrational modes and allowed the detection of the Raman modes of the TIR phase down to 7.4 GPa. However, at 5.2 GPa the Raman spectrum started to change with some new peaks becoming detectable while older peaks disappear; thus indicating a mixture of phases. Below 2 GPa, the peaks of the crystalline high-pressure phase disappear and the Raman spectrum becomes similar to that of the original α-Bi_2O_3 sample (see **Fig. 2**); thus indicating the recovery of the initial α phase on fully release of pressure.

In order to analyze the Raman scattering measurements of the TIR sample down to 2 GPa and check whether or not corresponds to the HPC phase, we have to take into account that HPC-Bi_2O_3 is a hexagonal phase which has two independent Bi atoms, one located at 6c and the other at 2b Wyckoff positions, and two O atoms located at two independent 6c Wyckoff positions **[37]**. As can be observed in **Fig. 1(b)**, the HPC structure maintains the BiO_6 units of the α phase (although more regular than the α phase), but the rotation of the BiO_5 pyramids results in BiO_7 units **[37,51]**. Similarly to the case of the

α phase, the HPC phase can be regarded as a laminar structure where a sublayer of Bi atoms and a double sublayer of O atoms are perpendicular to the *c* axis.

According to group theory, HPC-Bi_2O_3 is non-centrosymmetric with four formula units in its primitive cell and has a mechanical representation with 60 vibrational modes at the BZ centre **[66]**:

$$\Gamma = 7\mathrm{A}_1 + 3A_2 + 7B_1 + 3B_2 + 10\mathrm{E}_2 + 10\mathrm{E}_1 \quad (2)$$

being A_2, B_1 and B_2 silent modes, E_1 and E_2 Raman-active doubly degenerated modes, and A_1 and E_1 polar modes which are both Raman- and IR-active. Since one A_1 and one E_1 modes correspond to zero-frequency acoustic modes, one expects twenty five Raman-active modes ($\Gamma_{Raman} = 6\mathrm{A}_1 + 10\mathrm{E}_2 + 9\mathrm{E}_1$) and fifteen IR-active modes ($\Gamma_{IR} = 6\mathrm{A}_1 + 9\mathrm{E}_1$). On the other hand, due to the polar character of A_1 and E_1 modes, a splitting of transversal optic (TO) and longitudinal optic (LO) modes is expected, thus resulting a total of forty Raman-active modes and thirty IR-active modes; however, the TO-LO splitting in the HPC phase is probably very small for the same reason that has been already commented for the α phase.

Figure 8 shows the pressure dependence of the Raman-active mode frequencies of the TIR sample along with the theoretical calculations of the Raman-active mode frequencies for the HPC phase. The most intense experimental peaks at 71, 76, 188, 197 and 293 cm^{-1} at 22 GPa show frequencies and pressure coefficients similar to those of E_2^1, E_2^2, A_1^2, E_2^5 and E_2^6 modes of HPC-Bi_2O_3, respectively. Moreover, from 22.2 GPa to 6 GPa, the experimental pressure dependence of the frequencies of most of the vibrational modes of the TIR sample agree with the theoretical predictions for the modes of HPC-Bi_2O_3. Consequently, we can tentatively assign the TIR sample to the HPC phase and conclude that the

thermal annealing of amorphous Bi_2O_3 at 20 GPa to 200°C is enough to produce a partial TIR of the amorphous phase into the HPC phase.

A comparison of the Raman spectra of the α phase (**Fig. 2(a)**) with the TIR sample (**Fig. 7**) at similar pressures makes clear that the shape of the spectra is completely different. Noteworthy is the absence of Raman modes of the HPC phase in the high-frequency region below 500 cm^{-1} near the B_g^{14} mode of the α phase and the presence of the E_2^7 mode of the HPC in the frequency gap between 220 and 280 cm^{-1} corresponding to the A_g^8 and A_g^9 modes of the α phase. **Table II** lists the experimental frequencies and pressure coefficients of the Raman peaks attributed to the HPC phase and observed after the annealing at two different pressures: 22.2 GPa (the highest pressure) and 7.5 GPa (the lowest pressure only with the HPC phase). **Table II** also summarizes the calculated frequencies and pressure coefficients (only TO components) of the twenty-five Raman- and IR-active modes and the thirteen silent modes of HPC-Bi_2O_3 at the same two pressures. The tentative assignment of the Raman modes proposed in **Table II** is based on the frequencies and pressure coefficients of the peaks.

As we have already commented, on decreasing pressure from 6 to 2 GPa new peaks similar to those of the α phase are observed, thus suggesting a mixture of phases in the pressure interval. Furthermore, below 2 GPa only peaks of the α phase are observed, hence indicating the complete recovery of the initial phase. This result contrasts with the results of Locherer *et al.* who observed a reversible HP to HPC phase transition around 2 GPa **[37]**. The discrepancy between our results and those of Locherer *et al.* could be related to the relatively low-annealing temperature used in our experiment. While Locherer *et al.* used 900°C to anneal the sample, we effectively use 200°C which may be insufficient to produce a total TIR of the amorphous sample. Therefore, we postulate that the amorphous material remaining after the annealing, which returns to the original α phase, could constitute nucleation centers that guide the atoms of the HPC to recover the original α phase on

decreasing pressure. This hypothesis could be verified by performing annealing at higher temperatures but they are out of our present experimental capabilities.

In order to understand better the lattice dynamics of the HPC phase, we show in **Fig. 4(b)** the phonon dispersion curves and total and partial one-phonon DOS of HPC-Bi_2O_3 at 6.2 GPa. Noteworthy, our calculations at lower pressures yield negative frequencies, thus indicating that the HPC structure is dynamically unstable below 6.2 GPa. This result is in good agreement with our experimental observations that show the non-metastable character of the TIR phase at 1 atm and further support our tentative assignment of the TIR phase to the HPC phase. As it can be observed, the phonon dispersion curves of the hexagonal HPC phase are less complex than those of the monoclinic α phase and the DOS of the HPC phase shows more minima (near 300, 350, 390, 450, 540 cm^{-1}) than in the α phase. The contribution of atomic movements to the vibrational modes of the HPC phase is, on the other hand, similarly to the α phase. Up to 160 cm^{-1}, vibrational modes are dominated by the Bi displacement with a small contribution of the O. From 160 cm^{-1} to 300 cm^{-1}, vibrational modes are dominated by the O displacement with a small contribution of the Bi atoms. Finally, above 300 cm^{-1}, the vibration modes that are dominated by the O displacement.

Visualization of the *ab initio*-calculated vibrational modes of HPC-Bi_2O_3 at Γ with the J-Ice software **[67]** shows that at high frequencies we cannot clearly differentiate between stretching and bending modes corresponding to isolated molecular BiO_x units, like in the α phase. Hence, vibrational modes of the HPC phase show a high interaction between BiO_6 and BiO_7 polyhedra of the HPC phase in the same way as there is a strong interaction between BiO_5 and BiO_6 polyhedra in the α phase. In fact, the vibrational modes of the HPC phase can be classified in a similar way to those of the α phase: i) from 0 to 200 cm^{-1} they are lattice modes essentially related to the displacement of the Bi atoms; and ii) from 200 to 600 cm^{-1} the vibrational modes are mainly a combination of stretching and bending of Bi-O

units related to the displacement of the O atoms. An interesting observation is related to the mode E_2^2 of the HPC phase which is calculated to be near 70 cm^{-1} at 7.4 GPa. This mode is a shear mode between alternate Bi-O layers extended in the *ac* plane of the HPC structure (see **Fig. 1(b)**). Similar modes are the half-layer shear modes present in III-VI layered materials (GaS, GaSe and InSe). These modes have E_{1g}, E, E'' and E_1 (and also E_2) symmetry and are observed near 60 cm^{-1} in GaSe and 74 cm^{-1} in GaS at 1 atm in the polytypes β, γ, ε and δ, respectively **[73,74]**. Curiously, the α phase also has a half-layer shear mode; however, it corresponds to the B_u^2 mode near 70 cm^{-1} at 1 atm (see **Fig. 10 and Table III** in the Appendix); hence supporting the view that three dimensional α- and HPC-Bi_2O_3 phases have a pseudolayer-like structure as shown in **Fig. 1**.

Finally, on the basis of our results presented in this study and our previous work **[51]**, we want to propose an energy landscape for α-Bi_2O_3 at ambient temperature between 1 atm and 20 GPa as that depicted in **Fig. 9**. This type of qualitative interpretation was recently used to explain the PIA of Y_2O_3 nanoparticles **[75]**. At 1 atm, the α phase is more stable than the HPC phase and that the amorphous phase. In particular, our theoretical calculations estimate that the α phase is 0.8 eV more stable than the HPC phase at 1 atm (note that the HPC phase is not stable according to our calculations at 1 atm). At 20 GPa, the scenario is different: the HPC phase becomes 1.4 eV more stable than the α phase; however, the system does not have enough energy to overcome the energy barrier that separates the α and the HPC phase at room temperature. At this pressure, the lack of energy, coupled with the dynamical and mechanical instabilities (which are out of the scope of the present paper and will be reported elsewhere), make the amorphous phase the energetically more favorable structure. The energy barrier that separates the amorphous and the HPC phase at 20 GPa was partially transposed when temperature raise to ~200^oC (~0.04 eV), thus indicating that the barrier should be slightly higher than 0.04 eV. Finally, since on decrease pressure to 1 atm we completely recover the α phase this means that the ambient temperature

(~ 0.02 eV) is sufficient to transpose the energy barrier that separate the HPC and the amorphous phase from the α phase at 1 atm.

Conclusions

In this work we present an experimental and theoretical study of the vibrational properties of synthetic α-Bi_2O_3 powder under pressure. Experiments performed up to 25 GPa by means of Raman scattering measurements have been complemented with DFT-based total energy and lattice-dynamics *ab initio* calculations. In general, there is a good agreement between our experimental and theoretical results and with previous experimental results. It is noteworthy that the experimental and theoretical pressure dependence of some high-frequency Raman-active modes of α-Bi_2O_3 is non-monotonous due to the occurrence of several pressure-induced anticrossings of phonon branches with the same symmetry which are caused by the complex vibrational scenario of α-Bi_2O_3.

The PIA of α-Bi_2O_3 at room temperature occurs at 20 GPa and is reversible when pressure is released from 25 GPa to 1 atm. However, annealing of the amorphous sample at 22.2 GPa at 200^{o}C during 3h proved to be sufficient to produce a partial recrystallization of the amorphous phase. This result confirms that PIA of α-Bi_2O_3 at room temperature is a consequence of the inability of the α phase to undergo a phase transition to another crystalline phase because of the existence of a high kinetic energy barrier between the two structures. The frequencies and pressure dependencies of the Raman-active modes of the recrystallized sample and the recovery of α-Bi_2O_3 at 1 atm are consistent with the HPC nature of the recrystallized high-pressure phase.

Finally, we want to stress that this work allows the validation of the lattice-dynamics *ab initio* calculations on this complex compound, which are difficult to be validated with neutron or x-ray inelastic scattering techniques, and which can be used to evaluate many physical properties of bismite.

We hope the present work will promote further studies; in particular structural studies in order to: i) verify the HPC nature of the recrystallized amorphous sample; ii) determine better the conditions of observation of the metastable HP phase; and iii) study the mechanical and/or dynamical instability of the α-Bi_2O_3 structure in order to shed light into the mechanism of PIA in this complex compound.

ACKNOWLEDGEMENTS

This work has been supported by Brazilian Conselho Nacional de Desenvolvimento Científico e Tecnológico (CNPq) under project 201050/2012-9, by Ministerio de Ciencia e Innovación of Spain (MICINN) under the National Program of Materials (MAT2010-21270-C04-03/04) and the Consolider-Ingenio 2010 Program (MALTA CSD2007-0045) and by Generalitat Valenciana through projects GVA-ACOMP-2013-012 and Prometeo 2009/053.

APPENDIX

1. IR-active modes in α-Bi_2O_3

The pressure dependence of the calculated IR-active modes in α-Bi_2O_3 is shown in **Fig. 10**. The theoretical zero-pressure frequencies and pressure coefficients of the IR-active modes in α-Bi_2O_3 are summarized in **Table III**. Experimental values of IR-active frequencies at 1 atm are also shown for comparison.

References

1.- E. A. Kravchenko, and V. G. Orlov, Zeits. Naturf. A **49**, 418 (1994).

2.- A. I. Kharkovskii, V. I. Nizhankovskii, E. A. Kravchenko, and V. G. Orlov, Zeits. Naturf. A **51**, 665 (1996).

3.- H. A. Harwig, and A. G. Gerards, J. Solid State Chem. **26**, 265 (1978).

4- S. G. Tan, L. J. Li, Y. Liu, P. Tong, B. C. Zhao, W. J. Lu, Y. P. Sun, Phys. C – Superc. Appl. **483**, 94 (2012).

5.- P. Singh, A. Agarwal, S. Sanghi, N. Singh and S. Khasa, Physica B **436**, 64 (2014).

6.- H. Maeda, Y. Tanaka, M. Fukutumi, and T. Asano, Jpn. J. Appl. Phys. **27(2)**, L209 (1988).

7.- H. Zhang, C. X. Liu, X.L. Qi, X. Dai, Z. Fang, and S. C. Zhang, Nature Phys. **5**, 438 (2009).

8.- D. Hsieh, Y. Xia, D. Qian, L. Wray, F. Meier, J. H. Dil, J. Osterwalder, L. Patthey, A. V. Fedorov, H. Lin, A. Bansil, D. Grauer, Y. S. Hor, R. J. Cava, and M. Z. Hasan, Phys. Rev. Lett. **103**, 146401 (2009).

9.- Y. L. Chen, J. G. Analytis, J.-H. Chu, Z. K. Liu, S.-K. Mo, X. L. Qi, H. J. Zhang, D. H. Lu, X. Dai, Z. Fang, S. C. Zhang, I. R. Fisher, Z. Hussain, and Z.-X. Shen, Science **325**, 178 (2009).

10.- H. Lin, R. S. Markiewicz, L. A. Wray, L. Fu, M. Z. Hasan, A. Bansil, Phys. Rev. Lett. **105**, 036404 (2010).

11.- J. R. Jeffries, A. L. L. Sharma, P. A. Sharma, C. D. Spataru, S. K. McCall, J. D. Sugar, S. T. Weir, and Y. K. Vohra, Phys. Rev. B **84**, 092505 (2011).

12.- B. Rasche, A. Isaeva, M. Ruck, S. Borisenko, V. Zabolotnyy, B. Büchner, K. Koepernik, C. Ortix, M. Richter, and J. van den Brink, Nat. Mat. **12**, 422 (2013).

13.- P. Patnaik, Handbook of Inorganic Chemical Compounds, McGraw-Hill (2003).

14.- A. Cabot, A. Marsal, J. Arbiol and J. R. Morante, Sensors and Actuators B **99**, 74 (2004).

15.- S. S. Bhande, R. S. Mane, A. V. Ghule, and S. H. Han, Scripta Mat. **65**, 1081 (2011).

16.- A. Orera, and P. R. Slater, Chem. Mat. **22**, 675 (2010).

17.- P. Shuk, H. D. Wiemhofer, U. Guth, W. Gopel, and M. Greenblatt, Solid State Ionics **89,** 179 (1996) and references there in.

18.- V. V. Kharton, F. M. B. Marques, A. Atkinson, Sol. State Ion. **174**, 135 (2004).

19.- S. Hull, Rep. Prog. Phys. **67**, 1233 (2004).

20.- R. Li, D. Wang, L. Ge, S. He, H. Chen, L. Guo, Ceramics Int. **40**, 2599 (2014).

21.- F. H. Elbatal, Nucl. Instr. and Meth. in Phys. Res. B **254**, 243 (2007).

22.- A. Bajaj, A. Khanna, B. G. Chen, J. G. Longstaffe, U. -W. Zwanziger, J. W. Zwanziger, Y. Gómez, and F. González, J. Non-Cryst. Solids **355**, 45 (2009).

23.- N. Chanthima, J. Kaewkhao, C. Kedkaew, W. Chewpraditkul, A. Pokaipist, and P. Limsuwan, Prog. Nucl. Sci. Tech. **1**, 106 (2011).

24.- K. Won-in, S. Pongkrapan, and P. Dararutana, Mat. Sci. Forum **695**, 223 (2011).

25.- T. Maeder, Int. Mat. Rev. **58**, 3 (2013).

26.- S. Iyyapushpam, S. T. Nishanthi, D. P. Padiyan, Mat. Lett. **86**, 25 (2012).

27.- L. Cheng, Y. Kang, J. Alloys Comp. **585**, 85 (2014).

28.- G. Malmros, Acta Chem. Scand. **24**, 384 (1970).

29.- B. Aurivillius, and G. Malmros, Trans. R. Inst. Technol. **291**, 3 (1972).

30.- J. W. Medernach, and R. L. Snyder, J. Am. Ceram. Soc. 61, 494 (1978).

31.- H. A. Harwig, Z. Anorg. Allg. Chem. **444**, 151 (1978).

32.- H. A. Harwig, J. W. Weenk, Z. Anorg. Allg. Chem. **444**, 167 (1978).

33.- G. Gattow, and H. Schroder, Z. Anorg. Allg. Chem. **318**, 176 (1962).

34.- N. Cornei, N. Tancet, F. Abraham, and O. Mentré, Inorg. Chem. **45**, 4886 (2006).

35.- M. Drache, P. Roussel, and J. P. Wignacourt, Chem. Rev. **107**, 80 (2007).

36.- S. Ghedia, T. Locherer, R. Dinnebier, D. L. V. K. Prasad, U. Wedig, M. Jansen, and A. Senyshyn, Phys. Rev. B **82**, 024106 (2010).

37.- T. Locherer, L. Dasari, V. K. Prasad, R. Dinnebier, U. Wedig, M. Jansen, G. Garbarino, andT. Hansen, Phys. Rev. B **83**, 214102 (2011).

38.- M. Cardona, R. K. Kremer, R. Lauck, G. Siegle, A. Muñoz, and A. H. Romero, Phys. Rev. B **80**, 195204 (2009).

39.- J. Serrano, F. J. Manjón, A. H. Romero, A. Ivanov, M. Cardona, R. Lauck, A. Bosak, and M. Krisch, Phys. Rev. B **81**, 174304 (2010).

40.- J. Serrano, A. Bosak, M. Krisch, F. J. Manjón, A. H. Romero, N. Garro, X. Wang, A. Yoshikawa, and M. Kuball, Phys. Rev. Lett. **106**, 205501 (2011).

41.- R. J. Betsch, and W. B. White, Spec. Acta **34**, 505 (1978).

42.- Z. V. Popovic, C. Thomsen, M. Cardona, R. Liu, G. Stanisic, R. Kremer, and W. König, Sol. State Commun. **66**, 965 (1988).

43.- A. Crossley, P. R. Graves, and S. Myhra, Physica C **176**, 106 (1991).

44.- F. D. Hardcastle, and I. E. Wachs, J. Sol. State Chem. **97**, 319 (1992).

45.- S. N. Narang, N. D. Patel, and V. B. Kartha, J. Molec. Struc. **327**, 221 (1994).

46.- V. N. Denisov, A. N. Ivlev, A. S. Lipin, B. N. Mavrin, and V. G. Orlov, J. Phys.: Condens. Matter. **9**, 4967 (1997).

47.- A. B. Kuz'menko, E. A. Tishchenko, and V. G. Orlov, J. Phys.: Condens. Matter. **8**, 6199 (1996).

48.- A. B. Kuz'menko, E. A. Tishchenko, I. L. Sashin, M. N. Khlopkin, and V. G. Orlov, J. Low Temp. Phys. **105**, 861 (1996).

49.- C. Chouinard, and S. Desgreniers, Solid State Communication **113**, 125 (2000).

50.- D. A. Fredenburg, and N. N. Thadhani, J. Appl. Phys. **110**, 063510 (2011).

51.- A. L. J. Pereira, D. Errandonea, A. Beltrán, L. Gracia, O. Gomis, J. A. Sans, B. García-Domene, A. Miquel-Veyrat, F. J. Manjón, A. Muñoz, and C. Popescu, J. Phys.: Condens. Matter **25**, 475402 (2013).

52.- N. Binggeli, and J. R. Chelikowsky, Phys. Rev. Lett. **69**, 2220 (1992).

53.- V. V. Brazhkin, A. Lyapin, O. Stalgorova, E. Gromnitskaya, S. Popova, and O. J. Tsiok, J. Non-Cryst. Solids **212**, 49 (1997).

54.- M. H. Cohen, J. Íñiguez, and J. B. Neaton, J. Non-Cryst. Solids **602**, 307 (2002); idem, Eur. Phys. J. E **9**, 239 (2002).

55.- S. M. Sharma, and S. K. Sikka, Prog. Mater. Sci. **40**, 1 (1996).

56.- A. Debernardi, C. Urlich, M. Cardona, and K. Syassen, Phys. Stat. Sol. (b) **223**, 213 (2001).

57.- K. Syassen, High Press. Res. **28**, 75 (2008).

58.- F. Datchi, R. Le Toullec, and P. Loubeyre, J. Appl. Phys. **81**, 3333 (1997).

59.- P. Hohenberg, and W. Kohn, Phys. Rev. B **136**, 3864 (1964).

60.- P. E. Blöchl, Phys. Rev. B **50**, 17953 (1994).

61.- J. P. Perdew, A. Ruzsinszky, G. I. Csonka, O. A. Vydrow, G. E. Suseria, L. A. Constantin, X. Zhou, and K. Burke, Phys. Rev. Lett. **100**, 136406 (2008).

62.-I. Y. Sklyadneva, R. Heid, K. -P. Bohnen, V. Chis, V. A. Volodin, K. A. Kokh, O. E. Tereshchenko, P. M. Echenique, and E. V. Chulkov, Phys. Rev. B **86**, 094302 (2012).

63.- R. Vilaplana, et al. Physical Review B **84**, 184110 (2011).

64.- R. Vilaplana, et al., Physical Review B **84**, 104112 (2011).

65.- K. Parlinsky, Computer code PHONON. See: http:// wolf.ifj.edu.pl/phonon.

66.- E. Kroumova, M. I. Arroyo, J. M. Perez-Mato, A. Kirov, C. Capillas, S. Ivantchev, and H. Wondratschek, Phase Transitions **76**, 155 (2003).

67.- P. Canepa, R. M. Hanson, P. Ugliengo, and M. Alfredsson, J. Appl. Cryst. **44**, 225 (2011).

68.- J. Serrano, F. J. Manjón, A. H. Romero, F. Widulle, R. Lauck, and M. Cardona, Phys. Rev. Lett. **90**, 055510 (2003).

69.- V.L. Ginzzburg, A.P. Levanyuk, and A.A. Sobyanin, Phys. Rep. **57**, 151 (1980).

70.- L. Hsu, M.D. McCluskey, and J.L. Lindström, Phys. Rev. Lett. **90**, 095505 (2003).

71.- J. M. Besson, J. Cernogora, and R. Zallen, Phys. Rev B **22**, 3866 (1980).

72.- J. M. Besson, J. Cernogora, M. L. Slade, B. A. Weinstein, and R. Zallen, Physica B **105**, 319 (1981).

73.- A. Polian, K. Kunc, and A. Kuhn, Solid State Commun. **19**, 1079 (1976).

74.- A. Polian, J. C. Chervin, and J. M. Besson, Phys. Rev. B **22**, 3049 (1980).

75.- L. Piot, S. L. Floch, T. Cornier, S. Daniele, and D. Machon, J. Phys. Chem. C **117**, 11133 (2013).

Table I. Experimental and theoretical Raman mode frequencies and zero-pressure pressure coefficients of α-Bi_2O_3 at room temperature obtained by fitting to equation $\omega(P)= \omega_0+a\cdot P+b\cdot P^2$. Superscripts in the symmetry denote the ordering from low to high frequencies. Data obtained by Chouinard *et al.* with powder and single crystal samples are also shown for comparison. Frequencies and pressure coefficients of modes suffering anticrossings between 400 and 450 cm^{-1} were obtained from linear fits at low pressures.

Symmetry	Experimental			Theoretical			Chouinard *et al*. [**49**]			
	ω_0 (cm^{-1})	a (cm^{-1}/GPa)	b (cm^{-1}/GPa^2)	ω_0 (cm^{-1})	a (cm^{-1}/GPa)	b (cm^{-1}/GPa^2)	ω_0 (cm^{-1}) (Powder)	ω_0 (cm^{-1}) (single crystal)	a (cm^{-1}/GPa) (Powder)	a (cm^{-1}/GPa) (single crystal)
A_g^1	53(1)	0.36(2)	-0.014(1)	54	0.48(2)	-0.015(1)	54	56	0.09	0.13
B_g^1	58(1)	0.63(6)	-0.019(3)	64	0.44(1)	-0.012(1)				
B_g^2	60(1)	0.66(7)		69	0.06(4)		68	67	0.11	0.34
A_g^2	67(1)	0.50(5)	-0.016(3)	70	0.96(4)	-0.085(6)	61	59	0.17	0.44
A_g^3	83(1)	0.53(6)	-0.011(3)	82	0.83(2)	-0.024(1)	85	86	0.22	0.29
B_g^3	93(1)	1.67(9)		96	1.40(5)		95	94	1.36	1.15
A_g^4	93(1)	2.71(7)	-0.063(4)	97	2.71(3)	-0.078(2)		97		
B_g^4	102(1)	2.17(9)	0.038(6)	106	3.27(7)	-0.043(3)	105			
A_g^5	118(1)	1.57(5)	-0.023(3)	121	1.05(4)	-0.011(2)	120	121	0.88	0.90
B_g^5	138(1)	1.67(9)	-0.036(5)	142	1.75(4)	-0.031(2)	140	140	0.52	0.59
A_g^6				143	0.92(9)	-0.013(4)	144	144		
B_g^6	151(1)	2.24(2)		153	2.15(5)		153	153	1.83	2.07
B_g^7	156(1)			163	1.91(4)					
A_g^7	183(2)	0.24(11)	0.037(5)	179	0.27(2)	0.042(1)	185	184	0.65	0.86
B_g^8		1.61(12)		208	2.73(2)					
A_g^8	209(2)	5.21(6)		220	7.33(4)	-0.117(2)	212	210	4.39	4.58
A_g^9	279(3)	3.00(16)	0.032(8)	271	5.21(2)	-0.087(1)	280	278	3.03	2.79
A_g^{10}	313(3)	1.32(13)	0.081(7)	308	2.83(6)	-0.005(3)	315	310	2.44	2.54
B_g^9				310	1.43(9)	0.032(4)				
B_g^{10}				314	4.56(8)	-0.073(4)				
A_g^{11}	329(3)	3.01(21)	0.063(2)	324	3.11(38)	0.248(45)	334	330		
B_g^{11}				356	1.16(28)	0.322(33)				
A_g^{12}	409(3)	1.66(5)		395	2.29(5)		411	409		
B_g^{12}				420	0.86(22)			438		
A_g^{13}	443(3)	0.43(15)		427	0.60(20)		443	445		
B_g^{13}				431	-0.07(8)					
A_g^{14}	448(3)	-0.51(5)		437	-1.15(3)		450	451		
B_g^{14}	469(3)*	3.75(8)		449	3.46(11)					
A_g^{15}				502	3.14(8)	0.010(4)	474			
B_g^{15}	528(4)	2.14(22)	0.053(11)	517	3.49(10)	-0.021(5)	533			

* Raman mode not observed at 1 atm.

Table II. Experimental and theoretical Raman mode frequencies and pressure coefficients of HPC-Bi_2O_3 at 7.4 GPa and 22.2 GPa. Superscripts in the symmetry denote the ordering from low to high frequencies. Pressure coefficients were obtained by fitting to equation $\omega(P)= \omega_0+ a \cdot P$.

Symmetry	Experimental			Theoretical HPC-Bi_2O_3		
	ω (cm^{-1})		a (cm^{-1}/GPa)	ω (cm^{-1})		a (cm^{-1}/GPa)
	7.4 GPa	22.2 GPa		7.4 GPa	22.2 GPa	
B_2^{1*}				44.1	88.4	3.44(32)
A_2^{1*}				46.9	67.1	1.42(5)
E_2^1	64	71	0.54(2)	64.3	71.5	0.50(1)
E_2^2		76	0.52 (5)	70.0	79.4	0.70(2)
E_1^1	86	92	0.78(9)	83.7	104.1	1.83(20)
E_1^2	89		1.58(6)	91.7	108.5	1.21(4)
B_1^{1*}				93.8	105.0	0.78(3)
E_2^3	123	126	0.35(5)	100.9	123.1	1.67(8)
E_1^3	124	150	1.85(5)	122.6	157.8	2.36(3)
A_1^1	139		1.78(4)	130.6	154.4	1.78(6)
B_1^{2*}				142.2	160.1	1.25(4)
E_2^4				158.1	185.3	2.10(9)
B_1^{3*}				161.5	192.2	2.18(5)
E_1^4		169	1.35(10)	164.6	178.6	0.97(1)
A_1^2	164	188	1.72(3)	164.9	190.8	1.84(4)
E_2^5	176	197	1.47(4)	188.2	203.9	1.04(2)
B_2^{2*}				195.8	243.1	3.29(7)
A_1^3	217	247	1.91(6)	215.6	241.3	1.70(3)
E_1^5				223.6	260.0	2.44(3)
A_2^{2*}				251.8	311.4	4.20(9)
E_2^6		293	3.80(13)	252.0	306.3	3.93(11)
B_1^{4*}				257.9	295.9	2.67(5)
E_2^7	292	332	2.84(7)	290.0	334.9	3.11(3)
E_1^6				307.2	356.9	3.55(8)
A_1^4				336.8	373.8	2.62(3)
B_1^{5*}				343.7	385.0	2.75(6)
E_2^8	357	399	3.12(11)	352.8	395.6	2.95(3)
E_1^7	384	416	2.67(22)	380.0	426.7	3.40(6)
A_1^5	424	465	3.09(8)	410.8	453.6	3.02(7)
E_1^8				436.7	461.5	1.70(1)
E_2^9				442.8	467.7	1.72(1)
B_1^{6*}				464.8	513.3	3.41(8)
A_1^6	468	480	1.08(15)	466.3	479.8	0.88(3)
B_2^{3*}				493.7	561.2	4.65(7)
A_2^{3*}				515.2	580.2	4.55(7)
B_1^{7*}				529.1	553.5	1.69(3)
E_2^{10}				545.2	598.7	3.65(1)
E_1^9		604	3.74(6)	559.4	612.4	3.61(2)

*Silent modes

Table IIII. Theoretical zero-pressure IR-active mode frequencies and pressure coefficients of α-Bi_2O_3 obtained by fitting to equation $\omega(P)= \omega_0+a\cdot P+b\cdot P^2$. Superscripts in the symmetry denote the ordering from low to high frequencies. Frequencies obtained by Kuz'menko *et al*. with single crystal samples are also shown for comparison.

	Theoretical			Kuz'menko *et al*. **[47]**
Symmetry	ω_0 (cm^{-1})	a (cm^{-1}/GPa)	b (cm^{-1}/GPa^2)	ω_0 (cm^{-1})
A_u^1	42	0.26(6)	-0.015(1)	37
A_u^2	58	2.61(11)	-0.077(1)	58
B_u^1	59	0.10(5)		58
B_u^2	70	1.26(2)		
A_u^3	93	1.12(1)		99
A_u^4	105	2.74(8)	-0.080(1)	
B_u^3	110	3.64(14)	-0.085(1)	102
A_u^5	126	1.19(2)		130
B_u^4	145	1.65(5)		145
A_u^6	159	2.47(4)		153
B_u^5	184	2.17(3)		175
A_u^7	189	4.78(10)	-0.038(1)	185
B_u^6	192	5.19(2)	-0.079(1)	179
A_u^8	217	7.89(15)	-0.165(7)	209
B_u^7	225	3.93(6)	-0.066(3)	222
A_u^9	273	2.20(9)		280
B_u^8	283	2.35(7)		280
A_u^{10}	301	3.02(12)	-0.066(5)	314
B_u^9	345	2.67(6)	-0.046(3)	362
A_u^{11}	372	2.28(2)		
A_u^{12}	395	4.77(12)	-0.068(5)	
B_u^{10}	397	2.43(3)		
B_u^{11}	402	4.95(7)	-0.059(3)	401
A_u^{13}	457	-1.38(9)	0.179(4)	486
B_u^{12}	478	1.24(3)		414
A_u^{14}	512	1.90(5)		544
B_u^{13}	514	2.28(7)		504

Figure label

Figure 1 – (color online) (a) Crystalline structure of monoclinic α-Bi_2O_3 at ambient pressure and (b) hexagonal HPC-Bi_2O_3 at 6.2 GPa. Blue balls represent Bi atoms and red balls represent O atoms. The α phase has one Bi with five-fold coordination (Bi1 – green polyhedra) and another with six-fold coordination (Bi2 – blue polyhedra). The HPC phase has one Bi with seven-fold coordination (Bi1 – orange polyhedra) and another with six-fold coordination (Bi2 – orange polyhedra).

Figure 2 – (color online) (a) Room-temperature Raman spectra of α-Bi_2O_3 at selected pressures up to 25 GPa. (b) Pressure dependence of Raman-active modes of α-Bi_2O_3 during compression from 0 to 20 GPa. Symbols (lines) represent experimental (theoretical) data. Black (red) color corresponds to A_g (B_g) symmetry.

Figure 3 – (color online) (a) Pressure dependence of the experimental (symbols) and theoretical (lines) Ag-type Raman-active modes of α-Bi_2O_3 in the frequency range between 380 and 480 cm-1. (b) Pressure dependence of the theoretical (lines) B_g-type Raman-active modes of α-Bi_2O_3 in the frequency range between 380 and 480 cm-1. Dashed lines indicate the expected pressure behavior of theoretical lines in absence of phonon anticrossing.

Figure 4 – (color online) Calculated phonon–dispersion curves along high-symmetry directions and total and partial phonon density of states (DOS) for (a) α-Bi_2O_3 at 1 atm and (b) HPC-Bi_2O_3 at 6.2 GPa.

Figure 5 – (color online) Pressure dependence of the FWHM of selected Raman-active modes of α-Bi_2O_3.

Figure 6 – (color online) Room-temperature Raman spectra before (21.5 GPa) and after (22.2 GPa) annealing at 200 ^oC.

Figure 7 – Room-temperature Raman spectra of the TIR sample of Bi_2O_3 at selected pressures on downstroke from 22.2 GPa to 1 atm.

Figure 8 – (color online) Pressure dependence of Raman-active modes of the TIR sample of Bi_2O_3 during decompression from 22.2 GPa to ambient pressure. Symbols, red lines and black lines represent the experimental data, theoretical Raman modes of HPC phase and theoretical Raman modes of the α phase, respectively.

Figure 9 – (color online) Energy landscapes of α, HPC and amorphous phases of Bi_2O_3 at 1 atm (black line) and 20 GPa (red line).

Figure 10 – (color online) Pressure dependence of IR-active modes of α-Bi_2O_3 during compression from 0 to 20 GPa. Black and red lines represent A_u and B_u modes, respectively. Dashed black lines indicate the expected pressure behavior of some theoretical A_u modes in absence of phonon anticrossing.

Figure 1

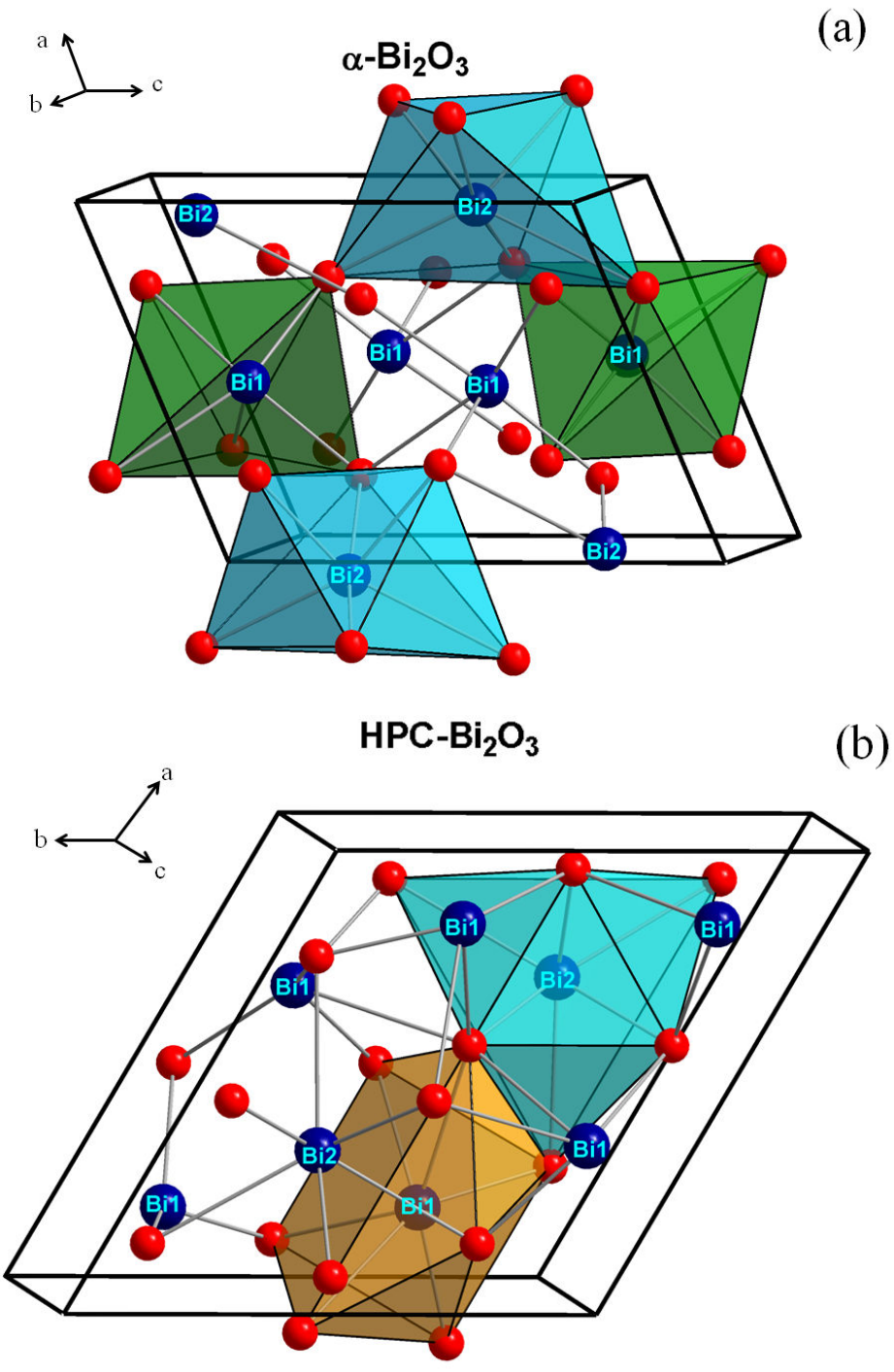
(a)
α-Bi2O3
a
b
c
Bi2
Bi2
Bi1
Bi1
Bi1
Bi2
Bi2
HPC-Bi2O3
(b)
a
b
c
Bi1
Bi1
Bi1
Bi2
Bi2
Bi1
Bi1

Figure 2(a)

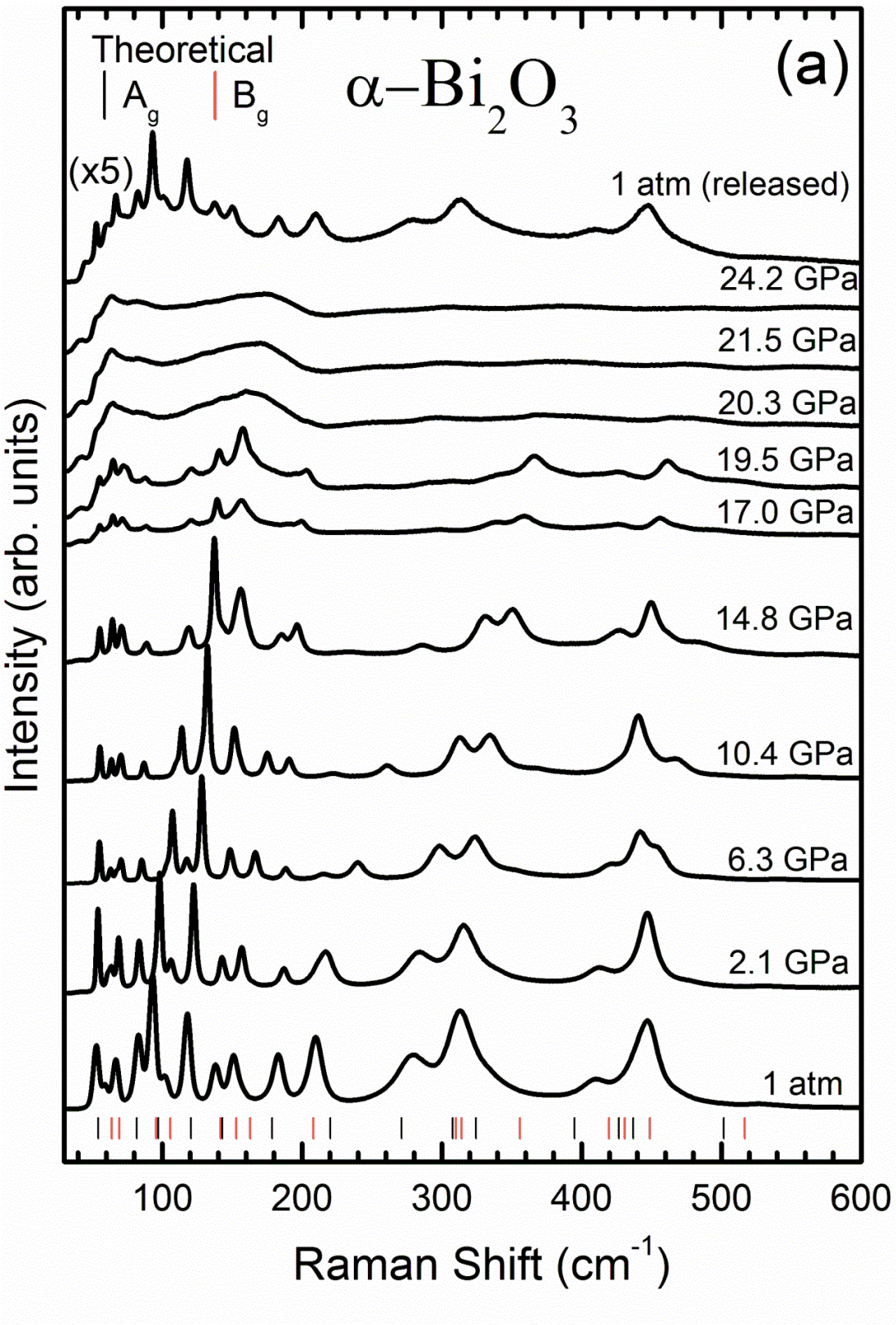
Theoretical
A_g
B_g
α–Bi2O3
(a)
(x5)
1 atm (released)
24.2 GPa
21.5 GPa
20.3 GPa
19.5 GPa
17.0 GPa
14.8 GPa
10.4 GPa
6.3 GPa
2.1 GPa
1 atm
Intensity (arb. units)
100
200
300
400
500
600
Raman Shift (cm-1)

Figure 2(b)

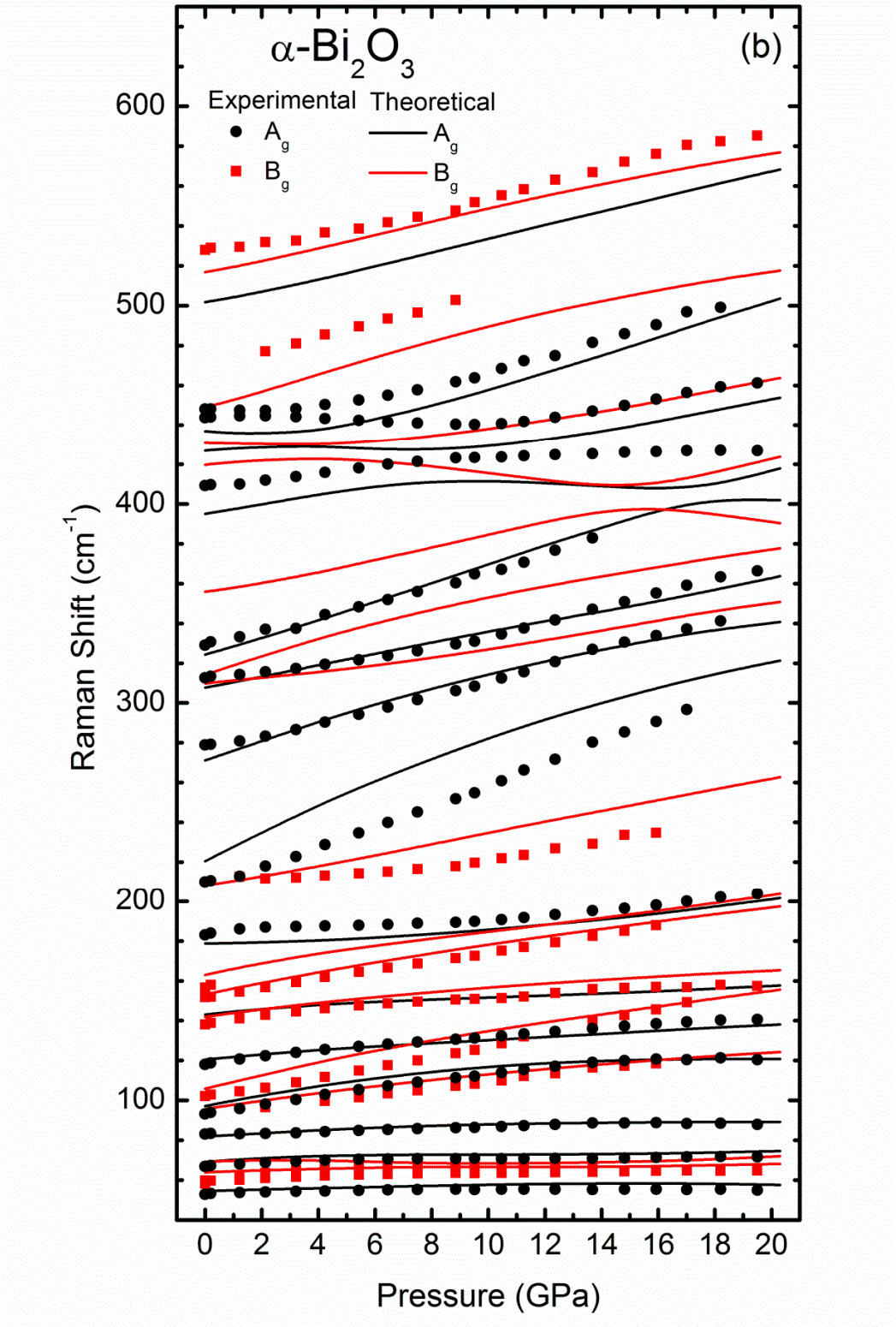
α-Bi2O3
(b)
Experimental
Theoretical
Ag
Bg
Ag
Bg
Raman Shift (cm-1)
Pressure (GPa)
100
200
300
400
500
600
0
2
4
6
8
10
12
14
16
18
20

Figure 3

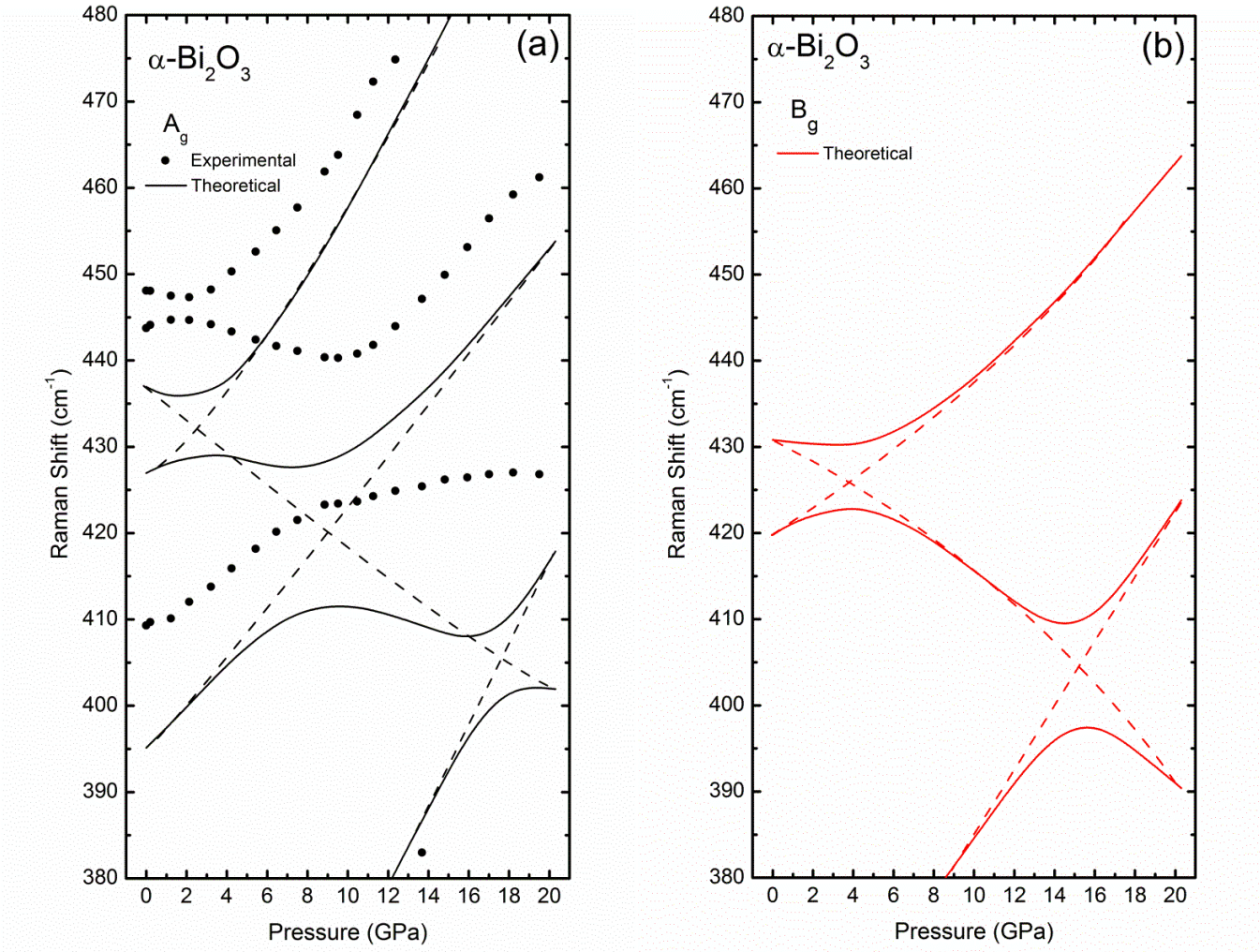
α-Bi2O3
(a)
Ag
Experimental
Theoretical
Raman Shift (cm-1)
Pressure (GPa)
α-Bi2O3
(b)
Bg
Theoretical
Raman Shift (cm-1)
Pressure (GPa)

Figure 4

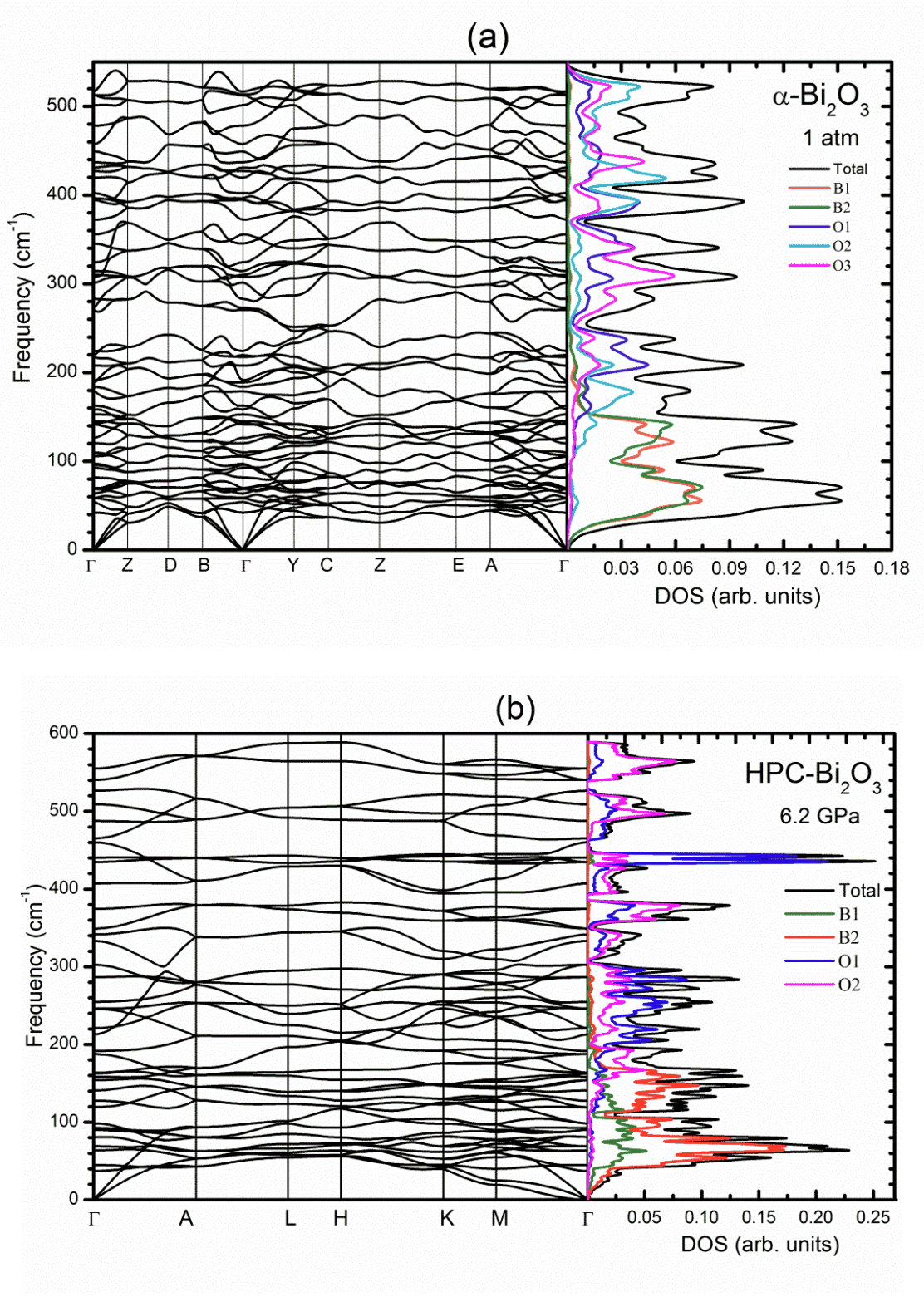
(a)
α-Bi2O3
1 atm
Total
B1
B2
O1
O2
O3
Frequency (cm-1)
0
100
200
300
400
500
Γ Z D B Γ Y C Z E A Γ
0.03 0.06 0.09 0.12 0.15 0.18
DOS (arb. units)
(b)
HPC-Bi2O3
6.2 GPa
Total
B1
B2
O1
O2
Frequency (cm-1)
0
100
200
300
400
500
600
Γ A L H K M Γ
0.05 0.10 0.15 0.20 0.25
DOS (arb. units)

Figure 5

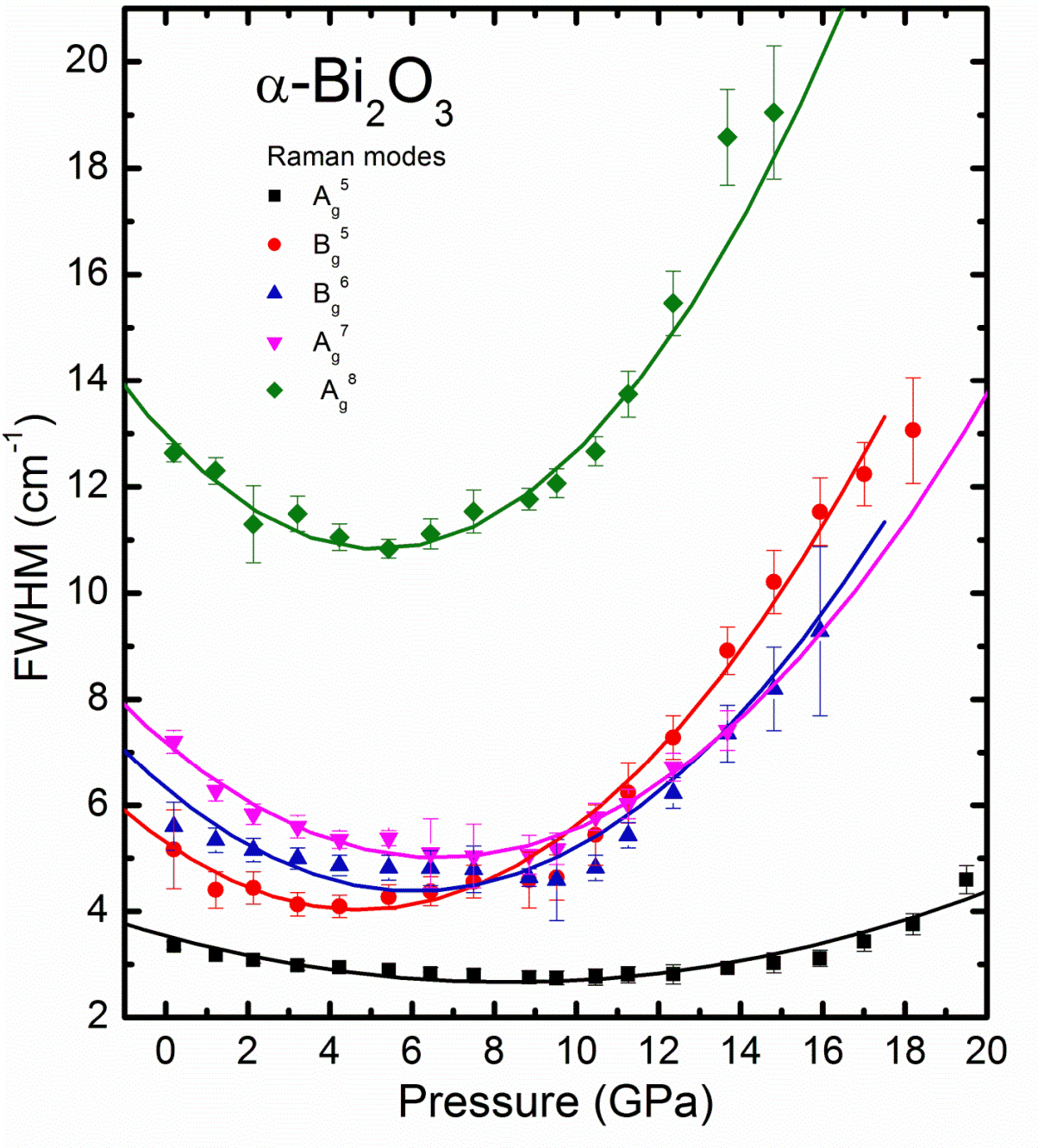
α-Bi2O3
Raman modes
Ag5
Bg5
Bg6
Ag7
Ag8
FWHM (cm-1)
Pressure (GPa)
0
2
4
6
8
10
12
14
16
18
20

Figure 6

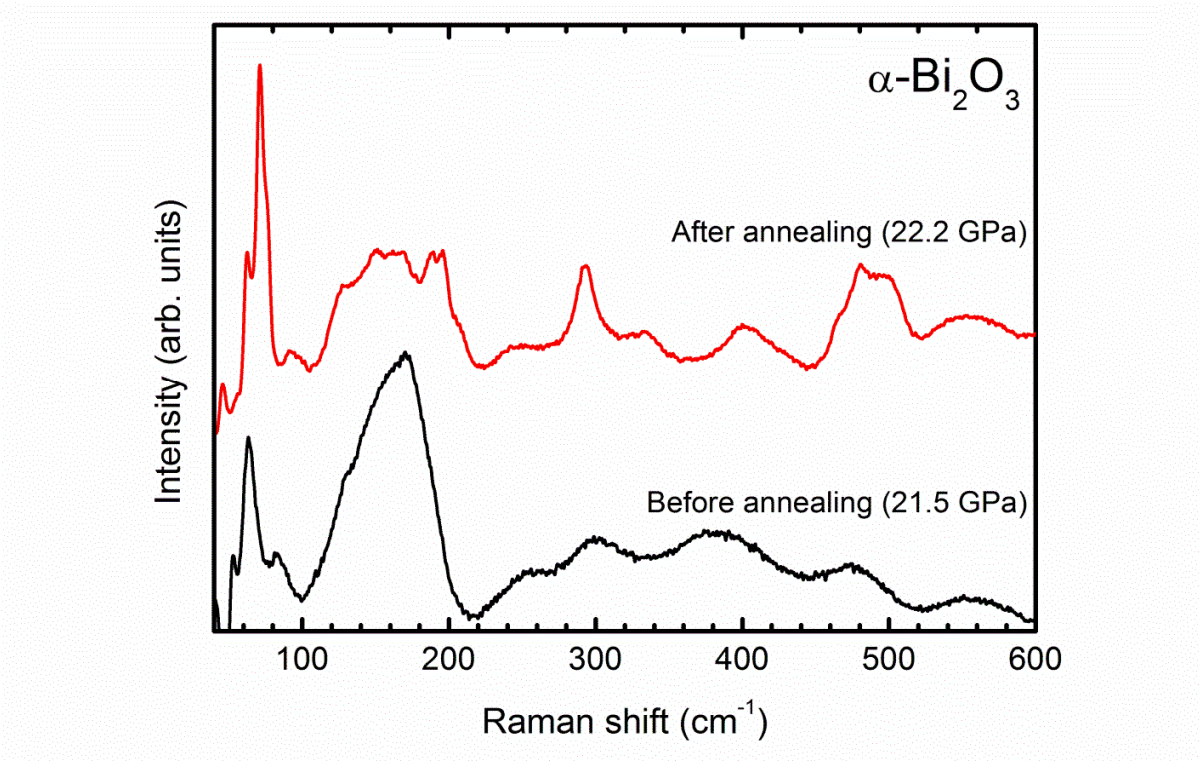
α-Bi2O3
After annealing (22.2 GPa)
Before annealing (21.5 GPa)
Intensity (arb. units)
100
200
300
400
500
600
Raman shift (cm-1)

Figure 7

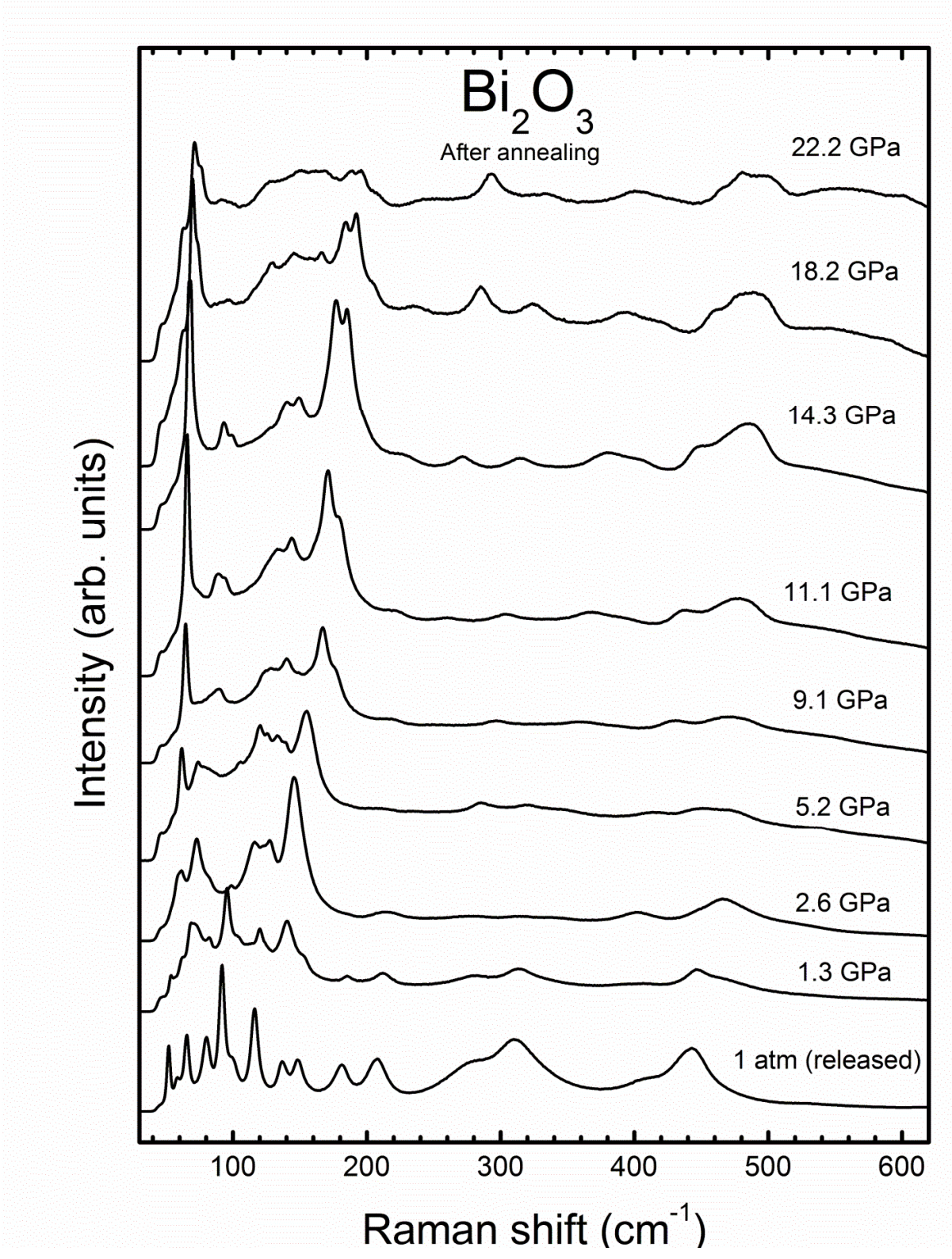
Bi2O3
After annealing
22.2 GPa
18.2 GPa
14.3 GPa
11.1 GPa
9.1 GPa
5.2 GPa
2.6 GPa
1.3 GPa
1 atm (released)
Intensity (arb. units)
100
200
300
400
500
600
Raman shift (cm-1)

Figure 8

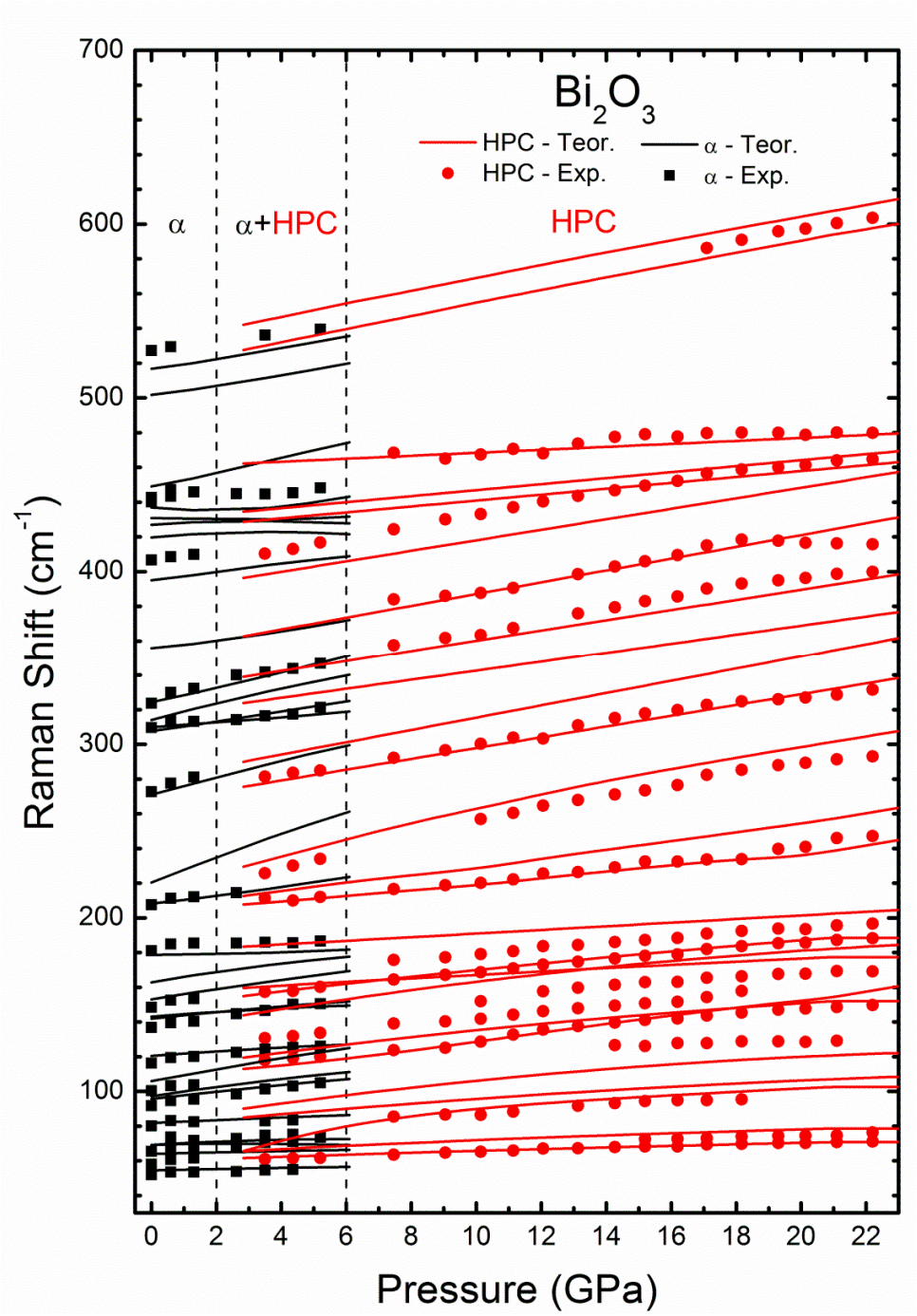
Bi2O3
HPC - Teor.
α - Teor.
HPC - Exp.
α - Exp.
α
α+HPC
HPC
Raman Shift (cm-1)
Pressure (GPa)
700
600
500
400
300
200
100
0
2
4
6
8
10
12
14
16
18
20
22

Figure 9

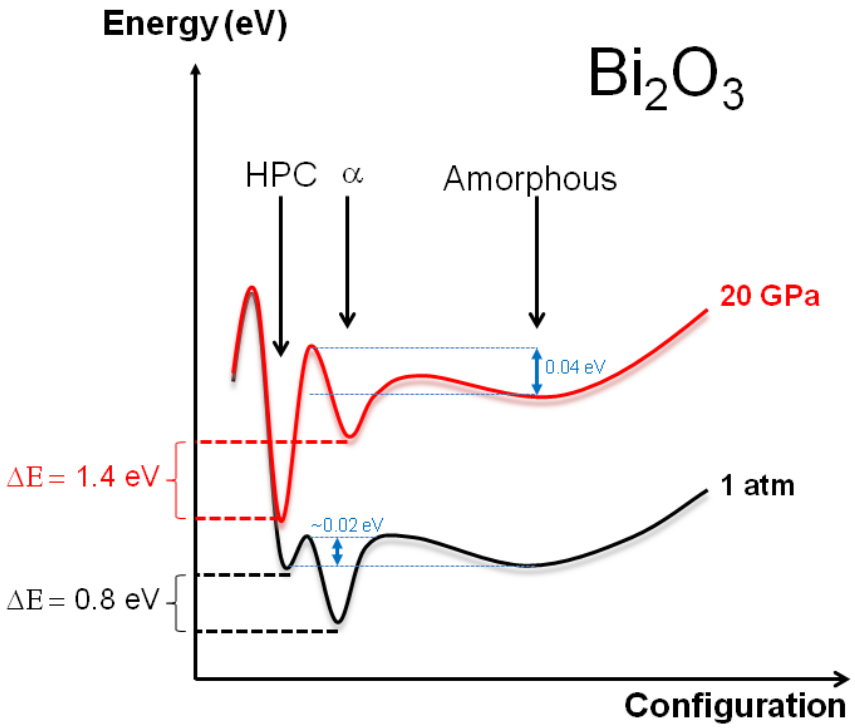
Energy (eV)
Bi_2O_3
HPC
α
Amorphous
20 GPa
0.04 eV
ΔE = 1.4 eV
1 atm
~0.02 eV
ΔE = 0.8 eV
Configuration

Figure 10

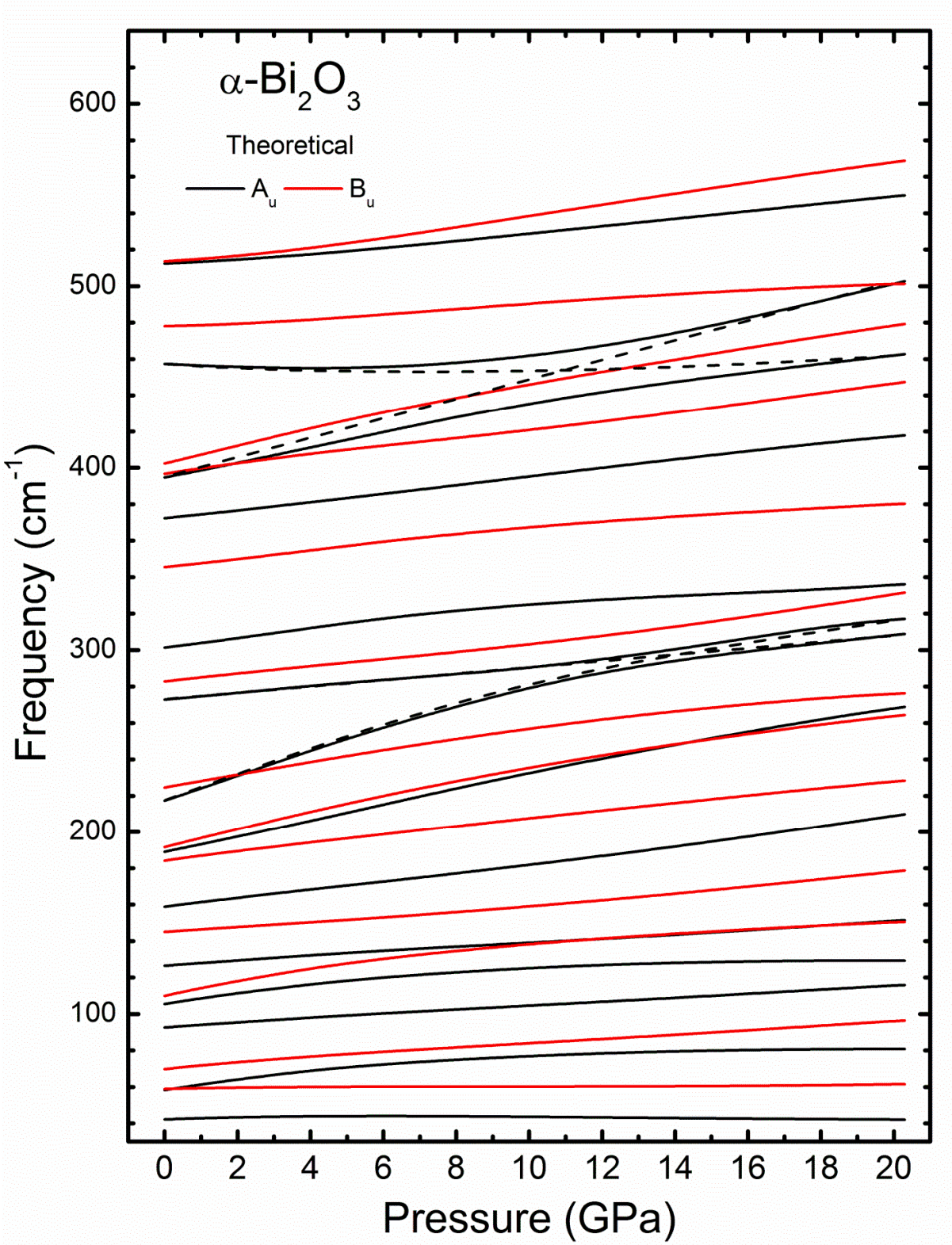
α-Bi2O3
Theoretical
Au
Bu
Frequency (cm-1)
Pressure (GPa)
600
500
400
300
200
100
0
2
4
6
8
10
12
14
16
18
20